Eur. Phys. J. E (2016) **39**: 51
DOI 10.1140/epje/i2016-16051-4

THE EUROPEAN PHYSICAL JOURNAL E

Regular Article

Mode instabilities and dynamic patterns in a colony of self-propelled surfactant particles covering a thin liquid layer[⋆,⋆⋆]

Andrey Pototsky[1], Uwe Thiele[2,3,a], and Holger Stark[4,b]

[1] Department of Mathematics, Faculty of Science Engineering and Technology, Swinburne University of Technology, Hawthorn, Victoria, 3122, Australia
[2] Institut für Theoretische Physik, Westfälische Wilhelms-Universität Münster, Wilhelm Klemm Str. 9, 48149 Münster, Germany
[3] Center of Nonlinear Science (CeNoS), Westfälische Wilhelms Universität Münster, Corrensstr. 2, 48149 Münster, Germany
[4] Institut für Theoretische Physik, Technische Universität Berlin, Hardenbergstrasse 36, 10623, Berlin, Germany

Received 21 December 2015
Published online: 6 May 2016 – © EDP Sciences / Società Italiana di Fisica / Springer-Verlag 2016

Abstract. We consider a colony of point-like self-propelled surfactant particles (swimmers) without direct interactions that cover a thin liquid layer on a solid support. The particles predominantly swim normal to the free film surface with only a small component parallel to the film surface. The coupled dynamics of the swimmer density and film height profile is captured in a long-wave model allowing for diffusive and convective transport of the swimmers (including rotational diffusion). The dynamics of the film height profile is determined by i) the upward pushing force of the swimmers onto the liquid-gas interface, ii) the solutal Marangoni force due to gradients in the swimmer concentration, and iii) the rotational diffusion of the swimmers together with the in-plane active motion. After reviewing and extending the analysis of the linear stability of the uniform state, we analyse the fully nonlinear dynamic equations and show that point-like swimmers, which only interact via long-wave deformations of the liquid film, self-organise in highly regular (standing, travelling, and modulated waves) and various irregular patterns.

1 Introduction

The self-organization of large numbers of microorganisms and artificial microswimmers and the non-equilibrium phase transitions that result from their collective behaviour are the focus of many recent theoretical and experimental studies [1,2]. Thus, in experiments with different types of artificial microswimmers, collective phenomena such as dynamic clustering, phase separation, and swarming are reported [3–7]. In experiments with suspensions of motile living cells (*e.g. E. coli* and *B. subtilis* bacteria or spermatozoa), a variety of regular and irregular large- and meso-scale density patterns is found [8–19]. With typical body sizes of several μm, the colonies of motile cells exhibit arrays of circular vortices, swirls, and meso-scale turbulence with correlation lengths between $\sim 10\,\mu$m and $\sim 100\,\mu$m. The emergence of large-scale coherent structures in systems composed of small self-propelled objects is universal and independent of the mechanism of motility. Thus, density waves with 50–100 μm wavelengths are observed in an assay of 1–10 μm long actin filaments, driven by motor proteins [20]. Stable networks of interconnected poles and asters are found in systems of microtubuli driven by kinesin complexes [21]. Similar to the suspensions of sea urchins spermatozoa [8], highly coherent arrays of circular vortices are found in motile assays of microtubulus, propelled by surface-bound motor proteins [22].

To explain the observed large-scale patterns, many theoretical models of interacting self-propelled particles are suggested and tested against experiments. One central question is to determine the driving force and the minimal conditions for the emergence of each of the observed patterns. One class of models are the so-called *dry* systems that neglect the motion of the embedding fluid medium [23–26]. In contrast, *wet* systems incorporate the motion and influence of the medium (*e.g.*, [27] and references therein). In dry systems density patterns form through a linear instability of the trivial homogeneous isotropic state. It is caused by the direct interaction between the particles, which is not mediated or induced by a solvent. For electrically neutral non-magnetic parti-

⋆ Contribution to the Topical Issue "Nonequilibrium Collective Dynamics in Condensed and Biological Matter", edited by Holger Stark, Marcus Baer, Carsten Beta, Sabine Klapp and Andreas Knorr.

⋆⋆ Supplementary material in the form of five .mp4 files and one .pdf file available from the Journal web page at
http://dx.doi.org/10.1140/epje/i2016-16051-4

[a] e-mail: u.thiele@uni-muenster.de
[b] e-mail: Holger.Stark@tu-berlin.de

cles, the interactions can be divided into two categories: steric effects (hard-core repulsion between colliding particles) [3,28–31] and long-range forces. They are introduced phenomenologically, like the aligning or anti-aligning interaction in Vicsek-type flocking models, [23, 25, 26] or are due to hydrodynamic [32, 33] or phoretic interactions [34,35].

Aligning interactions result from collisions between swimmers with elongated bodies [30, 36] or the bundling of flagellas of two colliding bacteria [15]. The origin of long-range anti-aligning interactions is not yet clear. For *wet* systems, the motion of the solvent gives rise to hydrodynamic interactions between the suspended particles [27] that at high densities may destabilize the polar order, *i.e.*, effectively act as a long-range anti-aligning force [10,37].

Presently, it is understood that the instability of a homogeneous suspensions of self-propelled particles can be induced by combining particle motility either with steric repulsion or with an aligning/anti-aligning interaction. At sufficiently high particle density, phase separation may occur in two-dimensional systems of repulsive finite-sized swimmers or self-propelled discs [3, 28]. This result is explained by the self-trapping of colliding swimmers, *i.e.*, any two swimmers that collide and swim against each other remain in contact for a certain time until their swimming directions have sufficiently changed. Also a mixture of short-range aligning and long-range anti-aligning interactions between point-like active Brownian particles leads to a rich variety of density and velocity patterns in dry systems with [25] and without [26] memory.

Here, we demonstrate that emergent collective dynamics in the form of persisting regular and irregular mesoscale density patterns is also found in colonies of self-propelled particles that do not interact directly. We consider active Brownian surfactant particles that move on the deformable surface of a thin liquid layer on a solid substrate. The swimming direction of each particle is assumed to have a non-zero vertical component, thus, leading to particles pushing against the film surface. Variations in the particle density give rise to large-scale film surface deformations that in turn induce flow in the layer of viscous fluid, which advects even more particles towards denser regions and also rotates their swimming directions. We assume that the swimmers act as a surfactant, *i.e.*, the local surface tension decreases with swimmer concentration. This results in a soluto-Marangoni effect, *i.e.*, Marangoni forces due to concentration gradients act at the free surface of the liquid film—they are a direct consequence of entropic contributions to the free energy of the surfactant-covered free surface [38]. As particle diffusion, the Marangoni forces act stabilizing by driving the liquid away from areas with increased particle concentration. Thus, in this system the interaction between the particles is indirect and is transmitted by the dynamics of the liquid layer.

The first model of swimmers on a liquid carrier layer was introduced in ref. [39]. There the particles are assumed to swim exclusively upwards and are not moving along the film surface by self-propulsion. Then the resulting excess pressure may cause a long-wave deformational instability of the film [39]. However, when one allows for lateral active motion of the swimmers [40] a sufficiently large swimming velocity and a moderate rotational diffusion strength can suppress this long-wave instability. Reference [40] confirms its linear stability results by hybrid (multiscale) discrete-continuous numerical simulations, while here we present the first fully nonlinear results for the continuum model.

The paper is organized as follows: In sect. 2 we derive the coupled long-wave evolution equations for the space- and time-dependent full swimmer density, which also includes swimmer orientation (Smoluchowski equation), and the space- and time-dependent film profile (thin-film equation). Next, we present a detailed linear-stability analysis of the trivial steady state. Different instability modes are discussed and located in a stability diagram spanned by rotational diffusion and self-propelling velocity. Section 4 discusses spatio-temporal patterns that emerge in the nonlinear regime. In particular, we analyse stable standing and travelling density waves accompanied by film modulation waves, travelling waves that are modulated by large-scale structures, and irregular patterns.

2 Motion of active Brownian swimmers at slowly deforming interfaces

We consider a 10–100 μm thin liquid film on a solid plate with a time-dependent film thickness profile $h(x, y, t)$. The deformable liquid-gas interface (shortly called "free surface") is covered by a colony of non-interacting active Brownian particles. Besides being microswimmers the particles act as insoluble surfactants [38,41,42] as often found for small particles [43]. In this way the particles are confined to move along the free surface and their density influences the interfacial energy of the free surface. The lower bound for the average film thickness of 10 μm is dictated by the typical size of self-propelling mono-cellular organisms such as *E. coli* or *the African trypanosome* [44], or artificial swimmers such as phoretically driven Janus particles (see, *e.g.*, [45, 46]). The typical size R of such swimmers is of the order of $R \approx 1\,\mu$m although recently much smaller swimmers of $R \approx 30$ nm have also been created [47]. We assume a dilute limit, where the average separation distance between the swimmers is much larger than their size. In this regime, direct two-particle interactions as well as hydrodynamic interactions can be neglected.

We start by deriving the equations of motion for an active Brownian particle that moves along a two-dimensional time-dependent surface profile $h(x, y, t)$, as shown schematically in fig. 1. The three-dimensional position vector of the particle is given by $\boldsymbol{r} = (x, y, h(x, y, t))$. The kinematic equation for the velocity reads

$$\dot{\boldsymbol{r}} = (\dot{x}, \dot{y}, \partial_t h + \dot{x}\partial_x h + \dot{y}\partial_y h). \tag{1}$$

For fixed surface shape, the velocity vector $\dot{\boldsymbol{r}}$ and the unit vector normal to the surface $\boldsymbol{n} = (-\partial_x h, -\partial_y h, 1)/\sqrt{1+(\partial_x h)^2+(\partial_y h)^2}$ are orthogonal to each other: $\dot{\boldsymbol{r}}\cdot\boldsymbol{n} = 0$.

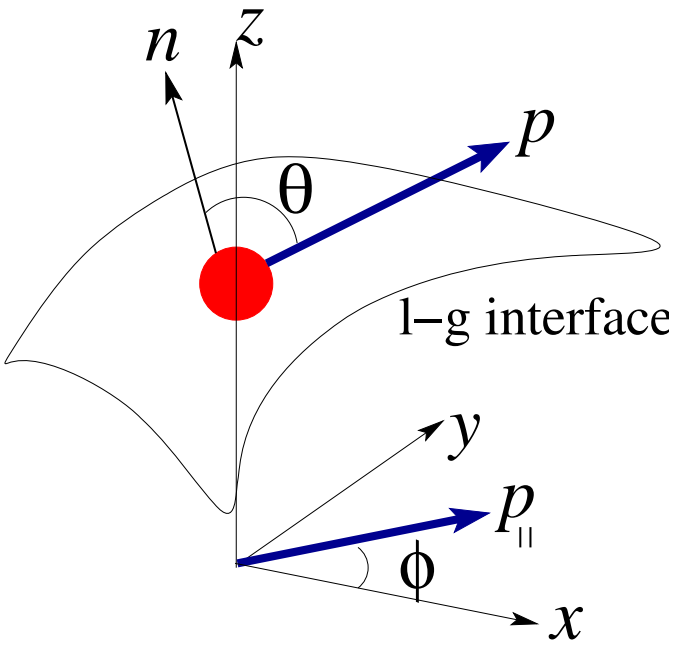

Fig. 1. (Color online) Detail of the liquid-gas interface with height profile $h(x, y)$ and with a single swimmer (filled circle). The instantaneous swimming direction is given by the vector $\boldsymbol{p}$ that makes an angle θ with the local normal $\boldsymbol{n}$. $\boldsymbol{p}_\parallel$ is the projection of $\boldsymbol{p}$ onto the (x, y) plane.

In the overdamped limit the total velocity of the particle moving along the interface $h(x, y, t)$ is given by the superposition of the local tangential components of the self-propulsion velocity $v_0\boldsymbol{p}_\tau$, the local tangential fluid velocity $\boldsymbol{u}_\tau$ of the film, the tangential component of the gravity force $\boldsymbol{g}_\tau = -g(\boldsymbol{e}_z)_\tau$, and thermal noise $\boldsymbol{\eta}_\tau(t)$, which results in diffusion along the free surface

$$\dot{\boldsymbol{r}} = v_0\boldsymbol{p}_\tau + \boldsymbol{u}_\tau + M\, m\boldsymbol{g}_\tau + \boldsymbol{\eta}_\tau(t). \tag{2}$$

Here, M denotes the mobility of the particle, m its effective mass, which is reduced due to buoyancy effects for partly submerged particles, and the unit vector $\boldsymbol{p}$ indicates the direction of swimming. Thermal noise is characterized by a Gaussian random variable with zero mean and correlation function $\langle\boldsymbol{\eta}(t)\boldsymbol{\eta}(t')\rangle = 2Mk_BT\delta(t - t')\mathbf{1}_2$, where k_B is the Boltzmann constant, T is the absolute temperature, and $\mathbf{1}_2$ is a 2×2 unit matrix. Note that the tangential component $\boldsymbol{a}_\tau$ of any vector $\boldsymbol{a}$ is given by

$$\boldsymbol{a}_\tau = \boldsymbol{a} - (\boldsymbol{a}\cdot\boldsymbol{n})\boldsymbol{n}\,. \tag{3}$$

Furthermore, the fluid velocity $\boldsymbol{u}$ at the free surface satisfies the standard kinematic boundary condition resulting from continuity [41]

$$\partial_t h = -u_x\partial_x h - u_y\partial_y h + u_z. \tag{4}$$

We consider particles swimming upward against gravity and pushing against the film surface. This already creates some polar order with a preferred vertical orientation of the swimmer bodies at the interface [48]. Further reasons for such a polar order can be bottom-heaviness [49], the chemotactic response of bacteria swimming towards the surface in order to take up oxygen [17], or any mechanism at the interface that aligns the particles along the vertical. In the following, we will not present a full derivation of the orientational distribution at the interface. Instead, for the distribution against the surface normal we will assume that it always adjusts instantaneously compared to the slow dynamics of the film interface (see below).

In what follows, we only take into account the long-wave deformations of the film surface, thus $\epsilon = h_0/\lambda \ll 1$, with λ the wavelength of the surface deformations and h_0 the average film thickness. By noticing that the in-plane gradient (∂_x, ∂_y) is of order ϵ, we obtain for the surface normal $\boldsymbol{n} = (0, 0, 1) + O(\epsilon)$ and for any vector $\boldsymbol{a}$ one has $\boldsymbol{a}_\tau = (a_x, a_y, 0) + O(a_z\epsilon) + O(a_x\epsilon) + O(a_y\epsilon)$, as it follows from eq. (3). Then, the Langevin equation (2) for the interfacial particle position becomes to leading order in ϵ

$$\begin{aligned}\dot{x} &= v_0\boldsymbol{p}_x + \boldsymbol{u}_x + \eta_x(t),\\ \dot{y} &= v_0\boldsymbol{p}_y + \boldsymbol{u}_y + \eta_y(t).\end{aligned} \tag{5}$$

Note that the tangential component of the gravity field vanishes in the long-wave limit, *i.e.* $\boldsymbol{g}_\tau = 0$.

The instantaneous orientation of swimmers is indicated by the three-dimensional unit vector $\boldsymbol{p}$, as shown in fig. 1. For swimmers in the bulk of the fluid, the time-evolution of $\boldsymbol{p}$ is well known: it is determined by the rotation due to local fluid vorticity, alignment against some external field such as gravity, and random rotation as controlled by rotational diffusivity D_r. However, for swimmers at a free surface, the rate of change $\dot{\boldsymbol{p}}$ may be significantly modified as compared to bulk swimmers depending on the nature of the interaction between the swimmers and the surface. For instance, a surface swimmer only partly submerged in the fluid and possibly with elongated body shape is easily rotated by local fluid vorticity within the film surface. However, the rotation of $\boldsymbol{p}$ against the interface normal is possibly reduced as the interaction energies strongly change similar to anchoring effects for liquid crystals.

Here, we use the argument from above to decouple the vertical component $\boldsymbol{p}_\perp$ of the orientation vector $\boldsymbol{p}$ from the in-plane component $\boldsymbol{p}_\parallel$. The evolution of the film surface is slow compared to the equilibration of $\boldsymbol{p}$ to a stationary distribution $P_s(\theta)$ with respect to the vertical. The mean of $\boldsymbol{p}_\perp$ is then given by

$$\langle\boldsymbol{p}_\perp\rangle = \int_0^\pi P_s(\theta)\cos\theta\sin\theta\,\mathrm{d}\theta, \tag{6}$$

whereas $\boldsymbol{p}_\parallel$ can vary according to the in-plane dynamics of $\boldsymbol{p}$, which couples to the temporal film evolution. Note that $P_s(0) > P_s(\pi)$, which implies that the swimmers push on average against the liquid-gas interface.

As a result, the rotation of $\boldsymbol{p}_\parallel$ is described in terms of the polar angle ϕ (see fig. 1)

$$\dot{\phi} = \frac{1}{2}\Omega_z + \chi(t), \tag{7}$$

where $\Omega_z = \partial_x u_y - \partial_y u_x$ is the vertical component of the local fluid vorticity and $\chi(t)$ is rotational noise with correlations $\langle \chi(t)\chi(t')\rangle = 2D_r\delta(t-t')$. Furthermore, we introduce the mean in-plane velocity of an active particle, $v_\parallel = v_0[1-\langle \boldsymbol{p}_\perp\rangle^2]^{1/2}$ and substitute $v_0\boldsymbol{p}_\parallel$ in eq. (5) by $v_\parallel \boldsymbol{q} = v_\parallel(\cos\phi, \sin\phi)$. Then, the Smoluchowski equation for the particle probability density $\rho(x,y,\phi,t)$, equivalent to eqs. (5) and (7), reads

$$\partial_t \rho + \boldsymbol{\nabla}\cdot\boldsymbol{J}_t + \partial_\phi J_r = 0, \tag{8}$$

where $\boldsymbol{\nabla} = (\partial_x, \partial_y)$ and the respective translational ($\boldsymbol{J}_t$) and rotational (J_r) probability currents become [40,50,51]

$$\begin{aligned}\boldsymbol{J}_t &= (v_\parallel \boldsymbol{q} + \boldsymbol{u}_\parallel)\,\rho - Mk_BT(\boldsymbol{\nabla}\rho),\\ J_r &= -D_r\partial_\phi\rho + \frac{1}{2}\Omega_z\rho.\end{aligned} \tag{9}$$

The swimmers and the liquid-gas interface couple through the local swimmer concentration $\rho(x,y,\phi,t)$ that acts twofold. First, each swimmer exerts the force $\alpha = v_0\langle p_\perp\rangle/M$ normal to the surface [39]. So, the total pushing force f_n per unit area is proportional to the total (direction-integrated) local concentration of swimmers, $\langle\rho\rangle(x,y,t) = \int_0^{2\pi}\rho(x,y,\phi,t)\,\mathrm{d}\phi$, *i.e.*,

$$f_n(x,y,t) = \alpha\langle\rho\rangle(x,y,t). \tag{10}$$

Second, the swimmers act as surfactant and change the local surface tension. Assuming a relatively low swimmer concentration, the surface tension σ is known to decrease linearly with $\langle\rho\rangle(x,y,t)$ [38],

$$\sigma = \sigma_0 - \Gamma\langle\rho\rangle, \tag{11}$$

with the reference surface tension σ_0 and $\Gamma > 0$.

Equations (10) and (11) couple the Smoluchowski equation (8) and the thin-film equation in the long-wave approximation [41] for the film thickness $h(x,y,t)$ [39,40],

$$\begin{aligned}\partial_t h + \boldsymbol{\nabla}\cdot\left(\frac{h^3}{3\mu}\boldsymbol{\nabla}\left[\sigma_0\Delta h - \rho_l g h + \alpha\langle\rho\rangle\right]\right)\\ - \Gamma\boldsymbol{\nabla}\cdot\left(\frac{h^2}{2\mu}\boldsymbol{\nabla}\langle\rho\rangle\right) = 0,\end{aligned} \tag{12}$$

where ρ_l is the density of the fluid and μ is its dynamic viscosity. The in-plane fluid velocity at the interface, $\boldsymbol{u}_\parallel = (u_x, u_y)$, is determined by the film profile $h(x,y,t)$ [41]

$$\boldsymbol{u}_\parallel = -\frac{\Gamma}{\mu}h\boldsymbol{\nabla}\langle\rho\rangle + \frac{h^2}{2\mu}\boldsymbol{\nabla}\left(\sigma_0\Delta h + \alpha\langle\rho\rangle\right), \tag{13}$$

and the vertical component of the vorticity is obtained as $\Omega_z = \partial_x u_y - \partial_y u_x$ from eq. (13)[1]. Both, $\boldsymbol{u}_\parallel$ and Ω_z enter the currents (9) that determine the Smoluchowski equation (8). Note, that without swimming along the interface and rotational diffusion, one can integrate this equation over ϕ to recover the model in ref. [39] with purely upwards pushing swimmers. Switching off the active swimming motion altogether one recovers the classical long-wave model for a dilute insoluble surfactant on a liquid film that may be written in a gradient dynamics form [38].

In what follows we focus on the instability induced by the pushing force generated by swimmers that swim predominantly upwards. To this end, we neglect the stabilising effect of the hydrostatic pressure $\rho_l g h_0$ as compared to the typical pushing force per unit area $\sim \rho_0 v_0/M$. Experimentally, such a regime can be achieved by using, for example, bacteria-covered water films with a dense bacterial coverage. In the dilute limit treated in this manuscript, one needs conditions of microgravity. To illustrate this example, we present some estimates. The maximal self-propulsion force of a unicellular bacterium is known to be of the order of several pN [52]. The maximal surface density ρ_0 is estimated as $\rho_0 \approx R^{-2}$, where $R \approx 1\,\mu$m is the typical size of the bacterial body. The dilute limit corresponds to densities of at least one order of magnitude below R^{-2}. Consequently, the maximal pushing force per unit area is estimated as $\rho_0 v_0/M \approx 10^{-1}$ (Pa). On the other hand, $\rho_l g h_0 \approx g\,10^{-2}$ (Pa) for a $10\,\mu$m thick water film. Clearly, $\rho_l g h_0$ can be neglected against $\rho_0 v_0/M$ in case of $g \ll 10\,\mathrm{m/s^2}$.

The possibility to experimentally detect the thin-film instability due to the pushing force α exerted by self-phoretic particles is further strengthened by recent experiments with $\sim 30\,$nm small Janus particles [47]. A much smaller particle size allows for larger surface particle densities and may give rise to larger excess pressure. In fact, the maximal density increases as $\sim R^{-2}$ for decreasing particle size R. However, it remains unclear how the pushing force α of a single self-phoretic particle scales with its size. If the decrease of the pushing force with R is slower than $\sim R^2$, the resulting excess pressure $\sim \rho_0 f$ exerted by the particles onto the liquid-gas interface can be several orders of magnitude larger than the value of $\approx 10^{-1}$ (Pa) estimated before in the dilute limit of a bacterial carpet.

For all what follows, we non-dimensionalise the evolution equations for film thickness $h(x,y,t)$ and swimmer density $\rho(x,y,\phi,t)$ employing the scaling as in ref. [40]. Thus, we use h_0 as the vertical length scale, $h_0\sqrt{\sigma_0/\Gamma\rho_0}$ as the horizontal length scale, $\mu h_0\sigma_0/(\Gamma^2\rho_0^2)$ as the time scale, and the direction-averaged density of swimmers in the homogeneous state ρ_0 as the density scale. This gives the relevant parameters of our model: the dimensionless in-plane self-propulsion velocity $V = v_\parallel\mu\sigma_0^{1/2}/(\Gamma\rho_0)^{3/2}$, the dimensionless in-plane rotational diffusivity $D = D_r h_0\mu\sigma_0/(\Gamma\rho_0)^2$, the translational surface diffusivity $d = k_BTM\mu/(h_0\rho_0\Gamma)$, and the excess pressure parameter $\beta = \alpha h_0/\Gamma$. Furthermore, we introduce the effective in-plane diffusivity

$$D_{\mathrm{eff}} = \frac{V^2}{2D} + d. \tag{14}$$

[1] Note that Ω_z can also be introduced as $\lim_{z\to h}(\boldsymbol{\nabla}\times\boldsymbol{u})_z$, where $(\boldsymbol{\nabla}\times\boldsymbol{u})_z$ denotes the vertical component of the fluid vorticity in the bulk of the film. The difference between $\lim_{z\to h}(\boldsymbol{\nabla}\times\boldsymbol{u})_z$ and $\partial_x u_y - \partial_y u_x$ with (u_x, u_y) from eq. (13) is of second order in the parameter ϵ of the long-wave approximation, and thus, does not affect the results of the linear stability of the homogeneous steady state. However, certain aspects of the nonlinear evolution may vary depending on the definition of Ω_z.

$$-\mathcal{J}(\boldsymbol{k}) = \left(\begin{array}{cc|ccccc} T_{11}, & T_{12}, & 0 & 0 & 0 & 0 & 0 & \dots \\ T_{21}, & T_{22}, & V^{(-)}, & V^{(+)}, & 0 & 0 & 0 & \dots \\ \hline 0 & V^{(+)}, & D+dk^2, & 0 & V^{(-)}, & 0, & 0 & \dots \\ 0 & V^{(-)}, & 0 & D+dk^2, & 0 & V^{(+)}, & 0 & \dots \\ 0 & 0 & V^{(+)}, & 0 & 2^2D+dk^2, & 0 & V^{(-)} & \dots \\ 0 & 0 & 0 & V^{(-)}, & 0 & 2^2D+dk^2, & 0 & \dots \\ 0 & 0 & 0 & 0 & V^{(+)}, & 0 & 3^2D+dk^2 & \dots \\ \dots & & & & & & & \end{array}\right), \tag{22}$$

Note that D_{eff} corresponds to the diffusion coefficient of a single self-propelled Brownian particle moving along a flat two-dimensional surface [53, 54]. In appendix A we summarize our non-dimensionalised dynamic equations.

3 Linear stability of homogeneously covered flat film

3.1 General

We present a more detailed stability analysis of the flat film than ref. [40] including an analytical treatment. We linearise the non-dimensionalised eqs. (8) and (12) about the homogeneous isotropic steady state ($h = 1$, $\rho = 1$) using the ansatz

$$h(x,y,t) = 1 + \delta h, \qquad \rho(x,y,\phi,t) = 1 + \delta\rho, \tag{15}$$

where $\delta\rho, \delta h \ll 1$. We obtain, respectively,

$$\partial_t \delta\rho + \boldsymbol{\nabla}\cdot(V\boldsymbol{q}\delta\rho) + \Delta\left[\left(\frac{1}{2}\beta - 1\right)\langle\delta\rho\rangle + \frac{1}{2}\Delta(\delta h)\right]\frac{1}{2\pi} - d\Delta\delta\rho - D\partial_\phi^2\delta\rho = 0, \tag{16}$$

$$\partial_t(\delta h) + \frac{1}{3}\left[\Delta^2(\delta h) + \beta\Delta\langle\delta\rho\rangle\right] - \frac{1}{2}\Delta\langle\delta\rho\rangle = 0, \tag{17}$$

with $\langle\delta\rho\rangle = \int_0^{2\pi}\delta\rho(x,y,\phi,t)\,\mathrm{d}\phi$. The linearised surface velocity $(\delta u_x, \delta u_y)$ from eq. (13) reads

$$\delta\boldsymbol{u}_\parallel = -\boldsymbol{\nabla}\langle\delta\rho\rangle + \frac{1}{2}\boldsymbol{\nabla}\left[\Delta(\delta h) + \beta\langle\delta\rho\rangle\right]. \tag{18}$$

As in ref. [40] we Fourier transform (FT) δh and $\delta\rho$ by using a continuous FT in space and a discrete FT in the angle ϕ. Combining this with an exponential ansatz for the time dependence we get

$$\delta h(\boldsymbol{r},t) = \int \hat{h}(\boldsymbol{k})e^{\gamma(\boldsymbol{k})t}e^{I\boldsymbol{k}\boldsymbol{r}}\,\mathrm{d}\boldsymbol{k},$$
$$\delta\rho(\boldsymbol{r},\phi,t) = \lim_{N\to\infty}\frac{1}{2\pi}\sum_{n=-N}^{N}e^{In\phi}\int W_n(\boldsymbol{k})e^{\gamma(\boldsymbol{k})t}e^{I\boldsymbol{k}\boldsymbol{r}}\,\mathrm{d}\boldsymbol{k}, \tag{19}$$

with the small dimensionless Fourier amplitudes $\hat{h}(\boldsymbol{k})$ and $W_n(\boldsymbol{k})$, the wave vector of the perturbation $\boldsymbol{k} = (k_x, k_y)$, and the real or complex growth rate $\gamma(\boldsymbol{k})$. Substituting eqs. (19) into eqs. (16), (17), we obtain the eigenvalue problem

$$\gamma(\boldsymbol{k})\mathbf{H} = \mathcal{J}(\boldsymbol{k})\mathbf{H}, \tag{20}$$

with the eigenvector $\mathbf{H}$

$$\mathbf{H}(\boldsymbol{k}) = (\hat{h}, W_0, W_1, W_{-1}, W_2, W_{-2}, \dots), \tag{21}$$

and the Jacobi matrix $\mathcal{J}$ of banded structure

see eq. (22) *above*

where $k^2 = k_x^2 + k_y^2$, $V^{(+)} = \frac{Vk_y}{2} + \frac{iVk_x}{2}$, $V^{(-)} = -\frac{Vk_y}{2} + \frac{iVk_x}{2}$. The (2×2) matrix $\boldsymbol{T}$ in the upper left corner of $\mathcal{J}$ is given by

$$\boldsymbol{T}(\boldsymbol{k}) = \begin{pmatrix} \frac{1}{3}k^4, & \left(\frac{1}{2} - \frac{\beta}{3}\right)k^2 \\ \frac{1}{2}k^4, & \left(1 - \frac{1}{2} + d\right)k^2 \end{pmatrix}. \tag{23}$$

Note that $\boldsymbol{T}$ coincides with the Jacobi matrix in ref. [39] that encodes the linear stability in the special case of purely upwards pushing swimmers. In practice, we truncate the expansion in the angle ϕ and only keep the first N Fourier modes. Then, $\mathcal{J}$ is a $(2N+2)\times(2N+2)$ matrix and the truncated eigenvector $\mathcal{H} = (\hat{h}, W_0, W_1, W_{-1}, \dots, W_N, W_{-N})$ is $(2N+2)$-dimensional. The stability diagram of the homogeneous isotropic state, as computed for reduced excess pressure $\beta = 4$ and translational diffusivity $d = 0.05$ from eqs. (20) is shown in fig. 2(a) in the parameter plane spanned by the reduced in-plane velocity V and the effective diffusion constant $D_{\text{eff}} = V^2/(2D) + d$ of the surfactants.

We numerically compute the eigenvalues of the truncated Jacobi matrix eqs. (22) for $N = 10$ and check the results by doubling to $N = 20$. The choice $\beta = 4$ and $d = 0.05$ corresponds to a flat film that is unstable at $V = 0$ as $\beta > \beta_c(d) = 2(1+d)$, the critical value for the onset of the long-wave instability [39], *e.g.*, $\beta_c = 2.1$ for $d = 0.05$. In what follows, we characterize the system by the parameters (V, D) and also indicate D_{eff}. As pointed out in ref. [40], for $\beta < \beta_c$ the trivial state is linearly stable regardless of the values of V and D. Recalling that $\beta = \alpha h_0/\Gamma$, where Γ is the Marangoni coefficient, we conclude that the soluto-Marangoni effect acts stabilizing.

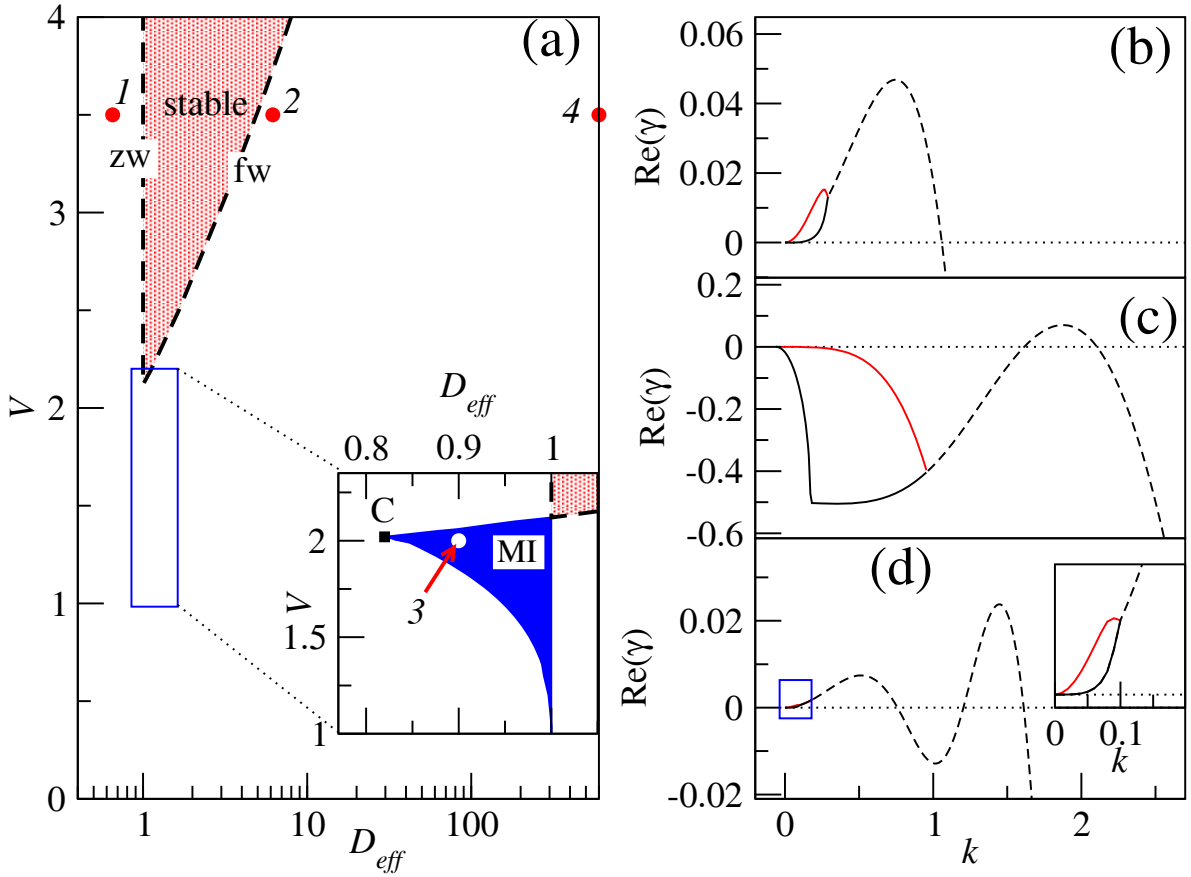

Fig. 2. (Color online) (a) Stability diagram of a flat film with homogeneous distribution of particles for $\beta = 4$ and $d = 0.05$. In the stable lightly shaded region $\mathrm{Re}[\gamma(k)] < 0$ for all values of the wave number k. The finite wave number instability sets in along the line marked by "fw". The zero-wave-number instability sets in along the vertical dashed line $D_{\mathrm{eff}} = 1$, marked by "zw". The inset zooms into the region marked by the rectangle in the main panel: In the strongly shaded area marked "MI", the mixed type fw/zw instability occurs. Panels (b-d) show $\mathrm{Re}[\gamma(k)]$ of the two leading eigenvalues for parameters taken (b) at point 1 ($V = 3.5$, $D = 10$, *i.e.*, $D_{\mathrm{eff}} = 0.66$), (c) at point 2 ($V = 3.5$, $D = 1$, *i.e.*, $D_{\mathrm{eff}} = 6.175$), and (d) at point 3 ($V = 2$, $D = 2.4$, *i.e.*, $D_{\mathrm{eff}} = 0.88$) in panel (a). Dashed and solid lines indicate complex and real eigenvalues, respectively. The inset in (d) zooms into the region marked by the rectangle.

For the system with non-zero in-plane velocity ($V \neq 0$), we have earlier reported the existence of two different instability modes [40]. Namely, for sufficiently large V, there exists a wedge-shaped stability region, marked in fig. 2(a) as "stable" that separates regions where the two different instability modes occur. The wedge opens at $V_c \approx 2.05$ towards larger values of V, *i.e.*, at any $V > V_c$, there exists a window in the effective diffusivity D_{eff} for which the flat homogeneously covered film is stable (note that V_c depends on β and d).

By crossing the two borders of the linearly stable region, the system changes stability via two distinct instability modes. The first mode corresponds to an oscillatory instability with a finite wave number at onset, *i.e.*, a travelling wave instability. In this case, for parameters directly on the stability threshold, the leading eigenvalue $\gamma(k)$ of the Jacobi matrix from eq. (22) has a negative real part for all values of the wave number k, except for the critical wave number $k_c \neq 0$, where $\gamma(k)$ has the form $\gamma(k_c) = \pm iW_c$ with some non-zero frequency W_c. We will refer to this instability mode as the finite wave number instability (fw). The second mode (zw) corresponds to an instability with a zero wave number at onset. This mode is characterized in detail in the next section.

3.2 Zero-wave-number instability: analytic results

In the following we present an approximate analytic expression for the zero-wave-number instability. We introduce the Fourier transformed fields $\delta\hat{h}(\boldsymbol{k}, t)$ and $\hat{\rho}(\boldsymbol{k}, \phi, t)$, according to $\delta h(\boldsymbol{r}) = \int e^{i\boldsymbol{k}\cdot\boldsymbol{r}} \delta\hat{h}(\boldsymbol{k}, t)\, \mathrm{d}\boldsymbol{k}$ and $\rho(\boldsymbol{r}) = \int e^{i\boldsymbol{k}\cdot\boldsymbol{r}} \hat{\rho}(\boldsymbol{k}, \phi, t)\, \mathrm{d}\boldsymbol{k}$, into eq. (16) and obtain

$$\partial_t \hat{\rho} + V\,(ik_x \cos\phi, ik_y \sin\phi)\,\hat{\rho} + \frac{1}{2\pi}\left(1 - \frac{\beta}{2}\right) k^2 \langle\hat{\rho}\rangle + \frac{1}{4\pi} k^4 (\delta\hat{h}) + d\,k^2 \hat{\rho} - D\partial_\phi^2 \hat{\rho} = 0. \tag{24}$$

Close to the threshold of the zero-wave-number instability, the amplitudes of all modes with the wave number $k \neq 0$ rapidly decay with time. Therefore, in the limit $k \to 0$,

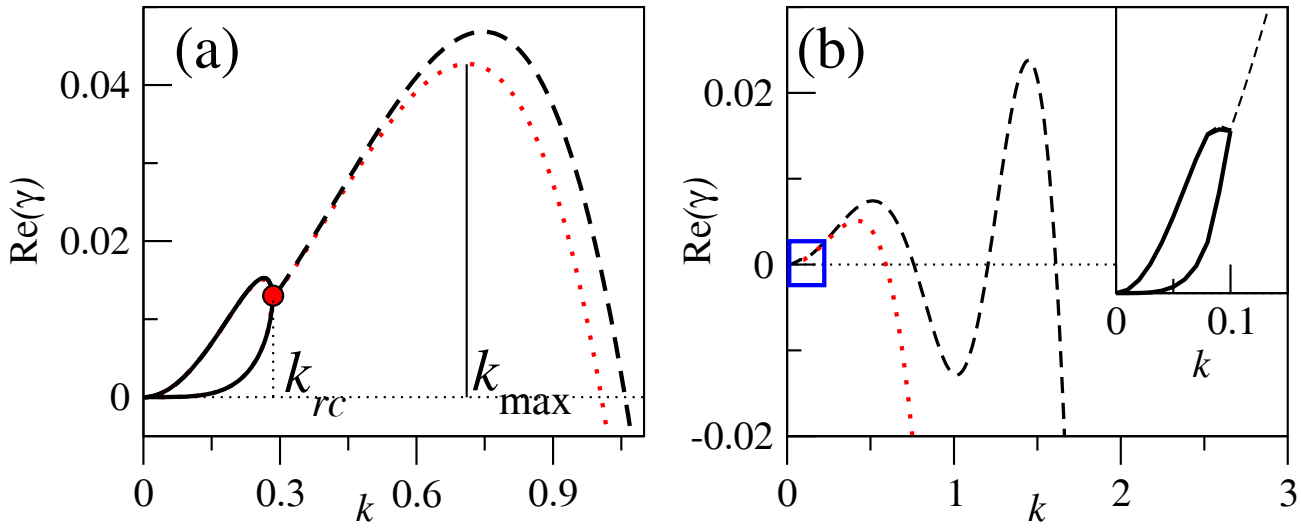

Fig. 3. (Color online) Comparison of the two leading numerically obtained eigenvalues of the full system (eq. (20), solid and dashed lines represent real and complex eigenvalues, respectively) and the analytic prediction for $k \ll 1$ (eq. (28), dotted lines). (a) $V = 3.5$, $D_{\rm eff} = 0.66$, (b) $V = 2$, $D_{\rm eff} = 0.88$. The inset zooms into the region marked by the rectangle, where the analytic and numerical results are indistinguishable from each other. The inset only shows the analytical eigenvalues.

in eq. (24) one may neglect the terms of orders k^2 and k^4 as compared to the ones of order k^0 and k. In consequence, the density and film height equations decouple. In fact, to this order the density equation describes a single self-propelled particle with rotational diffusivity D and self-propulsion velocity V but with neglected translational diffusivity.

To proceed further, we note that on length scales larger than the persistence length of an active particle, V/D, the dynamics becomes purely diffusive. To arrive at this result, one performs a multipole expansion of $\hat{\rho}(\boldsymbol{k}, \phi, t)$ in the angle ϕ using only the monopol $\langle\hat{\rho}\rangle$ and the dipole moment [34,55]. The latter can be elimated in the dynamic equation for $\langle\hat{\rho}\rangle$ and from eq. (24) one arrives at

$$\partial_t\langle\hat{\rho}\rangle + \left(1 - \frac{\beta}{2} + D_{\rm eff}\right) k^2\langle\hat{\rho}\rangle + \frac{1}{2}k^4\delta\hat{h} = 0, \qquad (25)$$

which is coupled to the linearised thin-film equation in Fourier space

$$\partial_t(\delta\hat{h}) + \frac{1}{3}\left[k^4\delta\hat{h} - \beta k^2\langle\hat{\rho}\rangle\right] + \frac{1}{2}k^2\langle\hat{\rho}\rangle = 0. \qquad (26)$$

Equations (25) and (26) are identical to the linearised equations for purely upwards swimming ($V = 0$) studied in ref. [39] when replacing the translational diffusivity by $D_{\rm eff}$. The Jacobi matrix $\boldsymbol{J}(k)$ corresponding to eqs. (25) and (26) is

$$\boldsymbol{J} = -k^2\begin{pmatrix} \frac{k^2}{3} & \frac{1}{2} - \frac{\beta}{3} \\ \frac{k^2}{2} & \eta \end{pmatrix}, \qquad (27)$$

where we introduced $\eta = 1 - \beta/2 + D_{\rm eff}$. The two eigenvalues $\gamma_1(k)$ and $\gamma_2(k)$ resulting when introducing the exponential time dependence are

$$\gamma_{1,2} = \frac{1}{2}\left(\mathrm{tr}(\boldsymbol{J}) \pm \sqrt{\mathrm{tr}(\boldsymbol{J})^2 - 4\det(\boldsymbol{J})}\right), \qquad (28)$$

with $\mathrm{tr}(\boldsymbol{J}) = -k^2[k^2/3 + \eta]$ and $\det(\boldsymbol{J}) = k^6(1/12 + D_{\rm eff}/3)$.

In fig. 3 we compare the analytic eigenvalues (eq. (28) with the two leading numerically obtained eigenvalues of the full system (eq. (20)). Solid (dashed) lines correspond to the numerically obtained real (complex) eigenvalues, respectively, dotted lines to eq. (28). Figure 3(a) is obtained for the parameters corresponding to point 1 in fig. 2(a), *i.e.*, $V = 3.5$ and $D_{\rm eff} = 0.66$, and fig. 3(b) corresponds to point 3 in fig. 2(b), *i.e.*, $V = 2$ and $D_{\rm eff} = 0.88$. In both cases, the agreement is excellent up to $k \approx 0.4$. Next, we use eq. (28) to classify the zero-wave-number instability that sets in along the dashed vertical line marked by "zw" in fig. 2(a). The real part of the leading eigenvalue changes its sign at $\eta = 0$, *i.e.*, at $D_{\rm eff} = \beta/2 - 1$. Thus, for $\beta = 4$ we obtain $D_{\rm eff} = 1$, in agreement with fig. 2(a).

In the unstable region ($\eta < 0$), the fastest growing wave number $k_{\rm max}$ always corresponds to a pair of complex conjugate eigenvalues (fig. 3(a)). By locating the maximum of $\mathrm{tr}[J(k)]$, we determine $k_{\rm max}$ and its complex growth rate,

$$k_{\rm max} = \sqrt{\frac{3}{2}|\eta|}\,, \qquad \mathrm{Re}[\gamma(k_{\rm max})] = \frac{3}{8}\eta^2,$$
$$\mathrm{Im}[\gamma(k_{\rm max})] = \pm\frac{|\eta|}{2}\sqrt{\frac{27}{2}|\eta|\left(\frac{1}{12} + \frac{D_{\rm eff}}{3}\right) - \frac{9}{16}\eta^2}. \qquad (29)$$

For $k < k_{\rm rc} < k_{\rm max}$, γ_1 and γ_2 are real. At

$$k_{\rm rc} = \sqrt{\frac{3\eta^2}{1 + 4D_{\rm eff} - 2\eta}} \approx \sqrt{\frac{3}{1 + 4D_{\rm eff}}}|\eta| \qquad (30)$$

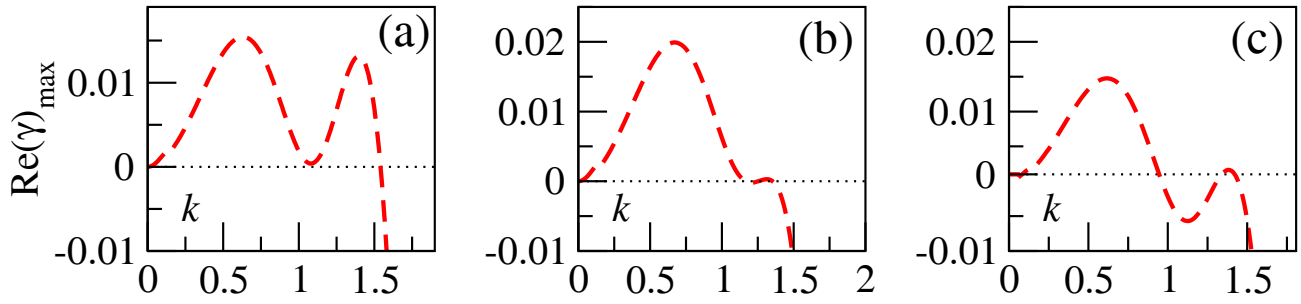

Fig. 4. (Color online) Transition from the finite wave number to the zero-wave-number instability region. Each panel shows the critical dispersion curve on the border of the MI region in fig. 2 at $D_{\text{eff}} < 1$. (a) $V = 2$, (b) $V = 2.0275$ (corresponding to the cusp point C in the inset of fig. 2(a)), and (c) $V = 2.03$.

the two real eigenvalues meet and become a pair of complex conjugate ones. One notes that this zero-wave-number instability is peculiar: Directly at onset ($\eta = 0$) the two leading eigenvalues are real, however, already arbitrarily close above onset ($\eta < 0$) the band of unstable wavenumbers contains a region of real modes (close to and including $k = 0$) and a region of complex modes (always including the fastest growing mode). This behaviour is related to the existence of two conserved fields, h and $\langle\rho\rangle$, that forces two real modes with zero growth rate at $k = 0$. The fastest growing wave number $k_{\max}$ tends to zero when approaching the stability threshold from above. Here, we call this scenario a zero-wave-number instability.

3.3 Mixed instability

The analytic results obtained in the previous section give for the zero-wave-number instability the threshold $D_{\text{eff}} = 1$ for $\beta = 4$. This perfectly agrees with the numerically computed threshold (left thick dashed line in fig. 2(a)). These results remain valid for small $V < V_c$ deep in the unstable region, *i.e.*, $\text{Re}[\gamma(k)]$ at $k \approx 0$ always changes from positive to negative as D_{eff} is increased past the critical value $D_{\text{eff}} = 1$ (at $\beta = 4$). However, there is always an instability at a non-zero wave number, as we explain next.

We observe a mixed-instability region, marked by "MI" and heavily shaded in the inset of fig. 2(a), where the system is unstable w.r.t. a finite- and a zero-wavelength instability, *i.e.*, there exist two bands of unstable wave numbers: one with $k \in [0, k_1]$ and another one with $k \in [k_2, k_3]$, with $k_3 > k_2 > k_1 > 0$. Dispersion relations for the zero wave number, the finite wave number, and the mixed instabilities, are shown in figs. 2(b), (c), and (d), respectively. The respective parameters are; point 1: $V = 3.5$, $D = 10$, *i.e.*, $D_{\text{eff}} = 0.66$, point 2: $V = 3.5$, $D = 1$, *i.e.*, $D_{\text{eff}} = 6.175$ in the main panel, and point 3: $V = 2$, $D = 2.4$, *i.e.* $D_{\text{eff}} = 0.88$ in the inset of fig. 2(a).

The transition from the finite wave number instability to the zero-wave-number instability can follow two scenarios. We identify them by keeping V constant and gradually decrease D_{eff}. In the first scenario for $V \gtrsim V_c = 2.05$, the maximum of $\text{Re}[\gamma(k)]$ in fig. 2(c) first becomes negative, *i.e.*, the finite wave number instability is stabilised while crossing the "fw" line in the stability diagram. Subsequently, the system crosses the "zw" line and becomes unstable w.r.t. the zero-wave-number mode. In the second scenario for $V \lesssim V_c = 2.05$, the system first crosses the line $D_{\text{eff}} = 1$ and enters the mixed instability region. Then the dispersion curve as in fig. 2(d) gradually transforms into the dispersion curve of the zero-wave-number instability, while leaving the region MI. Note that the mixed instability region stretches from $V = V_c$ down to $V = 0$. However, its horizontal width is negligibly small for $V < 1$.

The second scenario is visualised in fig. 4, where each panel shows the critical dispersion curve on the border of the MI region in fig. 2 at a certain value of $D_{\text{eff}} < 1$. For $V = 2$, the transition from the mixed instability to the zero-wave-number instability occurs through the elevation of the local minimum of the dispersion curve, so that a single band of unstable wave numbers emerges from the fusion of two such bands as shwon in fig. 4(a) for $D_{\text{eff}} = 0.83$. At the cusp marked by "C" in the inset of fig. 2(a), *i.e.*, at $V = 2.0275$, the transition occurs through the simultaneous elevation of the local minimum and the depression of the local maximum of the dispersion curve, as shown in fig. 4(b) for $D_{\text{eff}} = 0.81$. For $V = 2.03$ the transition occurs through the depression of the right local maximum of the dispersion curve (fig. 4(c) for $D_{\text{eff}} = 0.84$), so that the single band of unstable wave numbers emerges through the shrinking and vanishing of the second band.

4 Nonlinear evolution

4.1 Numerical approach and solution measures

Next we address the nonlinear evolution equations for film height $h(x, y, t)$ and density $\rho(x, y, \phi, t)$, which we give in non-dimensional form in eqs. (A.1) and (A.2) in appendix A. To solve them numerically, we discretize both fields on a square domain for the spatial coordinates $(x \in [-L/2, L/2]) \times (y \in [-L/2, L/2])$ and ρ additionally in the interval $\phi \in [0, 2\pi]$ for the orientation angle always using periodic boundary conditions (BC). We use $N = 100$ or $N = 128$ mesh points for each spatial direction to discretise space and 20 Fourier modes for the ϕ-dependence. We adopt a semi-implicit pseudo-spectral method for the

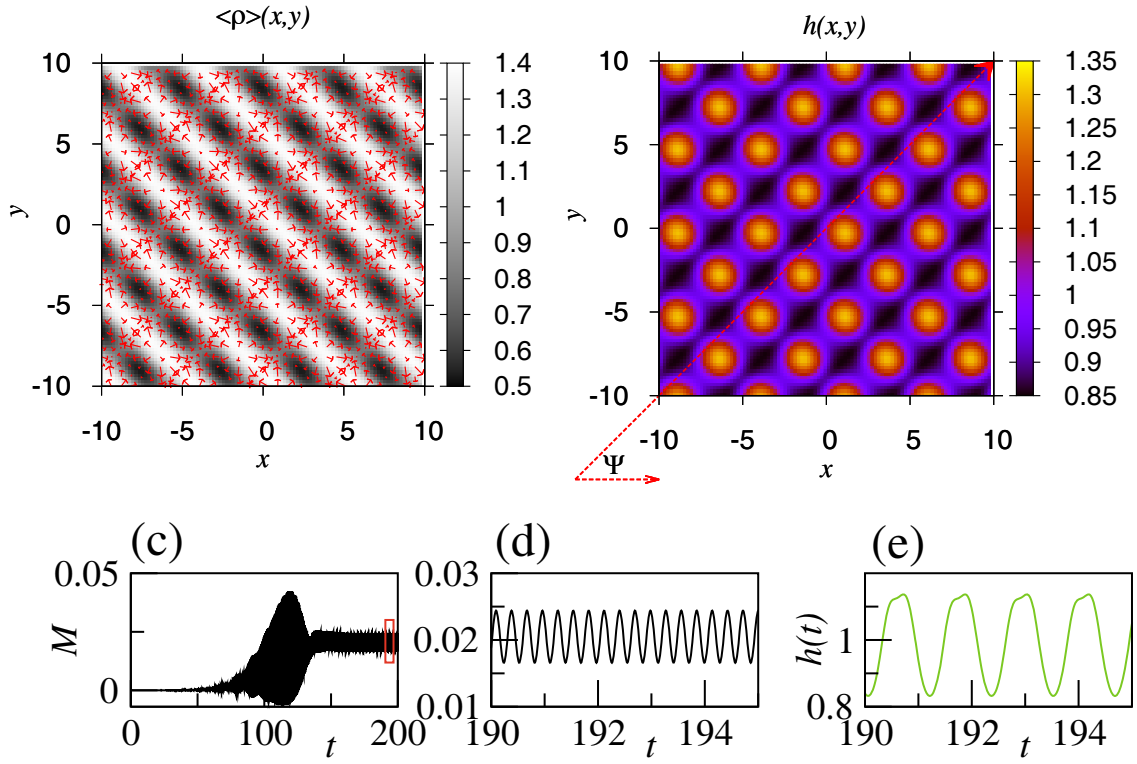

Fig. 5. (Color online) Standing wave pattern, obtained for $V = 3.5$, $D = 1$, $d = 0.05$, *i.e.*, $D_{\text{eff}} = 6.175$ (the corresponding dispersion curve is shown in fig. 2(c)). The snapshots are taken at $t = 190$: (a) average density $\langle\rho\rangle(x, y)$ (grey scale map) with average orientation field (red arrows) and (b) the film thickness $h(x, y)$. Ψ is the angle between the main lattice direction and the horizontal axis. Plotted *versus* time are: (c) The mode type M from eq. (31), (d) zoom of the region in (c) marked by the red rectangle, and (e) local film thickness $h(t)$ at a randomly chosen point on the surface.

time integration, as outlined in appendix A and verify selected results by using a fully explicit Euler scheme with $\Delta t = 10^{-4}$ or 10^{-5}. Note that the semi-implicite pseudo-spectral method remains stable for a significantly larger time step $\Delta t = 10^{-3}$.

To quantify the spatio-temporal patterns in film height and density, we introduce three global measures: the mode type

$$M = L^{-2} \iint (h(x, y, t) - 1)(\langle\rho\rangle(x, y, t) - 1)\mathrm{d}x\mathrm{d}y \quad (31)$$

determines if spatial modulations of $h(x, y, t)$ and $\langle\rho\rangle(x, y, t)$ are predominantly in-phase ($M > 0$) or anti-phase ($M < 0$). The space-averaged fluid flux

$$\bar{\boldsymbol{J}}_h = L^{-2} \iint \left(\frac{h^3}{3} \boldsymbol{\nabla} \left[\Delta h + \beta \langle\rho\rangle \right] - \frac{1}{2} \left(h^2 \boldsymbol{\nabla} \langle \boldsymbol{\rho} \rangle \right) \right) \mathrm{d}x\mathrm{d}y \quad (32)$$

distinguishes between standing waves ($\bar{\boldsymbol{J}}_h = 0$) and travelling or modulated waves ($\bar{\boldsymbol{J}}_h \neq 0$). Finally, the space-averaged translational flux of the swimmers

$$\bar{\boldsymbol{J}}_t = L^{-2} \iint \left(V \langle \rho \boldsymbol{q} \rangle + \boldsymbol{U}_{\parallel} \langle \rho \rangle \right) \mathrm{d}x\mathrm{d}y, \quad (33)$$

indicates global surface motion of the swimmers. In the following we indicate the richness in the dynamics of our system by giving examples of evolving patterns for specific parameter sets located in the stability diagram of fig. 2(a). Mapping out a full state diagram is beyond our present scope.

4.2 Regular standing wave pattern

We first study the parameters $V = 3.5$ and $D = 1$ ($D_{\text{eff}} = 6.175$) at point 2 in the unstable region of the phase diagram fig. 2(a), close to the finite wave number instability threshold. The corresponding dispersion curve is shown in fig. 2(c). The system size $L = 20$ is set to be several times larger than the fastest growing wave length $2\pi/k_{\max} = 3.43$. By numerically integrating eqs. (A.1), we study the temporal evolution of the system from the trivial state ($h = 1$, $\rho = 1/(2\pi)$). The initial conditions are $h = 1 + \delta h(x, y)$ and $\rho = 1/(2\pi) + \delta\rho(x, y, \phi)$, where the small perturbations $\delta h(x, y)$ and $\delta\rho(x, y, \phi)$ represent two independent sources of white noise.

We find that after a transient of $\approx$ 100 to 200 time units, the system settles onto a stable standing wave, that oscillates between different square and stripe patterns as Movie-1 in the Supplementary material shows. The mean fluid flux is zero, $\bar{J}_h = 0$. Figures 5(a) and (b) show a snapshot at time $t = 190$ of $\langle\rho\rangle(x, y)$ in gray scale together with the average orientation field $\langle \boldsymbol{q} \rangle = (\langle\cos\phi\rangle, \langle\sin\phi\rangle)$ as red arrows and $h(x, y)$, respectively. The patterns are

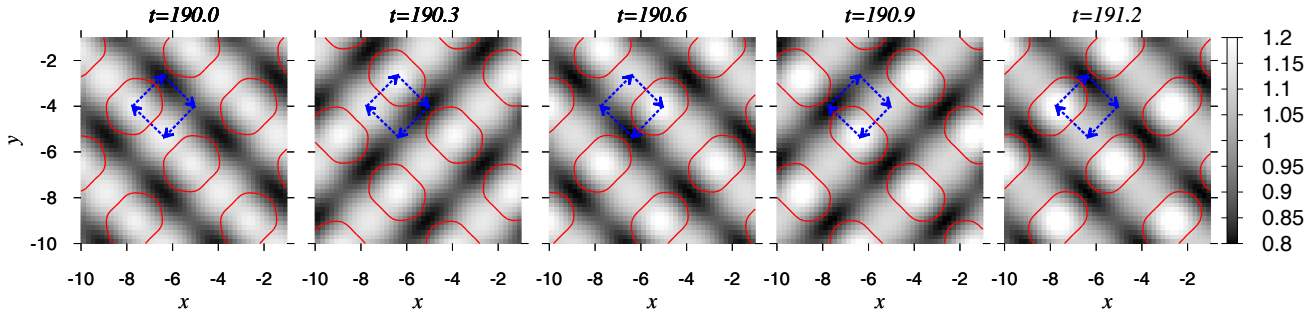

Fig. 6. (Color online) Standing stripe patterns with periodically changing directions for the same parameters as in fig. 5. Shown is a small portion of the square domain in fig. 5 over one oscillation cycle with period $T = 1.15$. Five snapshots of the film thickness $h(x, y, t)$ (in grey scale map) are plotted together with a contour plot of the average density $\langle\rho\rangle$ at the level of $\langle\rho\rangle = 1$. Arrows indicated the shift vector of the pattern during the four phases of one oscillation cycle.

highly dynamic, with h and $\langle\rho\rangle$ changing periodically in time, as analyzed in fig. 6. Figure 5(b) captures a moment in time during the change in stripe orientation from one diagonal to the other. In this phase individual maxima in $h(x, y, t)$ occur, that are arranged in a perfect square lattice, tilted by the angle $\Psi \approx \pi/4$ w.r.t. the x-axis.

The time evolution of the mode type M is plotted in fig. 5(c). After 150 time units M starts to oscillate periodically about the average $\overline{M} = 0.02$, as indicated in fig. 5(d), where a zoom of fig. 5(c) is shown. As $M > 0$, the oscillations of h and $\langle\rho\rangle$ are in-phase. The temporal period T of the standing wave is determined by observing the perfectly periodic oscillations of $h(t)$ at a randomly chosen point (fig. 5(e)). The period is $T = 1.15$.

Remarkably, the oscillations of M in fig. 5(d) are four times faster than the oscillations in film thickness. This is due to the fact that a complete period of the standing wave consists of four phases, where the same spatial pattern reappears four times, each time shifted along one side of a square and rotated by 90°. As M is invariant under rotation and translation of the pattern, its oscillation period is a quarter of the period of the standing wave. The four shifted and rotated patterns are clearly seen in Movie-1 in the Supplementary material when concentrating on the square lattice of side length l_w formed by the maxima in the height profile. In fig. 6 we illustrate the four phases by snapshots of the transient stripe patterns. During the first phase, the maxima of $\langle\rho\rangle$ and h shift along a straight line by a distance $l_w/2$. Each shift occurs along the direction orthogonal to the previous shift. After completing all four phases, the maxima have traveled along the sides of a square of side length $l_w/2$ back to their initial position. Between the square patterns the film thickness assumes patterns of parallel ridges that then decay into the square pattern and reappear rotated by $\pi/2$. One may say that during one cycle the pattern oscillates through several accessible patterns that are well known solutions for pattern forming systems on a square. In particular, they are known to occur as (stable or unstable) steady states in thin-film equations that describe "passive" liquid layers, ridges and drops on homogeneous solid substrates [56]. Appendix B gives further details regarding the measurement of the side length of the square pattern and the possible tilting angles Ψ of the pattern.

4.3 Strongly perturbed square pattern

Next, we study persisting patterns that emerge from the trivial state far from the stability threshold using $V = 3.5$, $D_{\text{eff}} = 600$ (point (4) in fig. 2(a)). The trivial state is linearly unstable w.r.t. the finite wave number instability with a dispersion relation similar to fig. 2(c). In a simulation in the square domain ($L = 20$) after a transient of about 20 time units, a state evolves which is highly dynamic and represents an underlying square pattern that is strongly perturbed by irregular temporal and spatial variations (see Movie-2 in the Supplementary material). Snapshots in fig. 7 show $h(x, y)$ and $\langle\rho\rangle(x, y)$ at $t = 100$. The latter varies between $\langle\rho\rangle_{\min} = 0.1$ and $\langle\rho\rangle_{\max} = 4.5$, in a much larger range than for the regular pattern in fig. 5. One recognizes the underlying square pattern in $\langle\rho\rangle(x, y)$ but the main lattice directions are tilted against each other. The profile $h(x, y)$ seems even stronger perturbed although the elevated regions (drops) are still approximately arranged on a square lattice. Movie-2 of the Supplementary material shows how the tilted lattice planes in $\langle\rho\rangle(x, y)$ seem to split up and merge with their neighbors. The snapshot in fig. 7 shows this scenario when going from left to right.

The evolution of the pattern is visualized in fig. 8(a)–(d). The mode type M in plot (a) is positive and oscillates randomly about $\overline{M} \approx 0.08$. In fig. 8(b) we plot the spectral density $S(\nu)$ of $M(t)$ calculated on the interval $t \in [20, 100]$. We find a clear maximum at the frequency $\nu_{\max} \approx 1.87$ with small width $\Delta\nu/\nu_{\max} \approx 0.1$, which corresponds to a period of $T = 1/\nu_{\max} \approx 0.53$. The frequency $\nu_{\max}$ belongs to the pulsating pattern clearly recognizable in Movie-2. A second, broader peak is located at $\nu_{\max} \approx 2.3$ with width $\Delta\nu/\nu_{\max} \approx 0.2$. In addition, there exists a continuous background in $S(\nu)$, which gives the pattern its random dynamic appearance. Random oscillations of the magnitude of the fluid flux, $|\bar{J}_h| = \sqrt{(\bar{J}_h)_x^2 + (\bar{J}_h)_y^2}$, (see fig. 8(c)) and of the magnitude of the translational flux of the swimmers, $|\bar{J}_t| = \sqrt{(\bar{J}_t)_x^2 + (\bar{J}_t)_y^2}$, (see fig. 8(d)), indicate persistent global propagation of the pattern. However, we find that the propagation direction randomly changes with time without preferred direction.

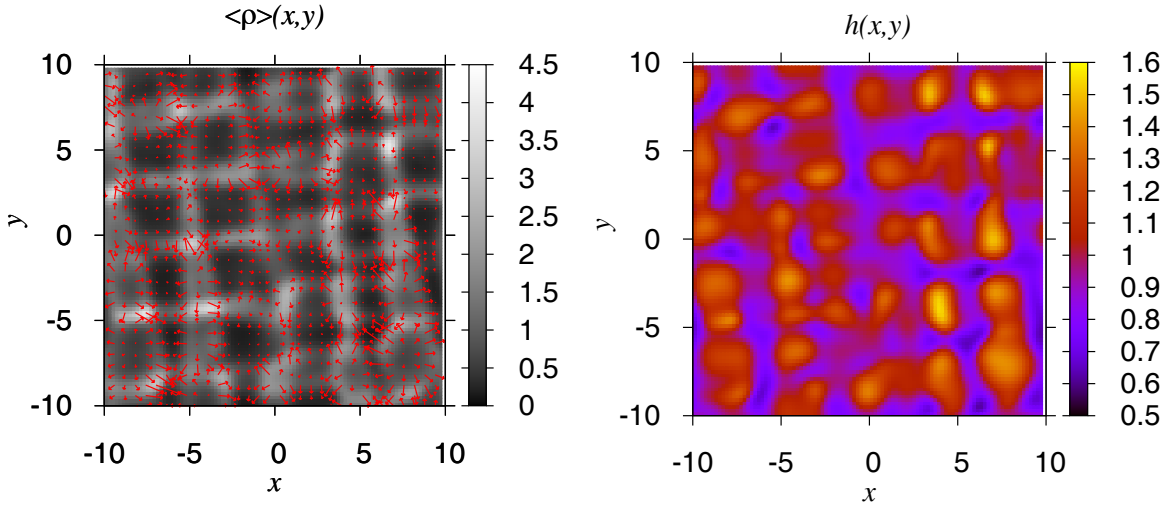

Fig. 7. (Color online) Example of a strongly perturbed square pattern at $V = 3.5$ and $D = 0.01$, *i.e.*, $D_{\text{eff}} = 600$ for a domain size $L = 20$. The temporal evolution started from the homogeneous state with random noise added. Snapshot is taken at $t = 100$.

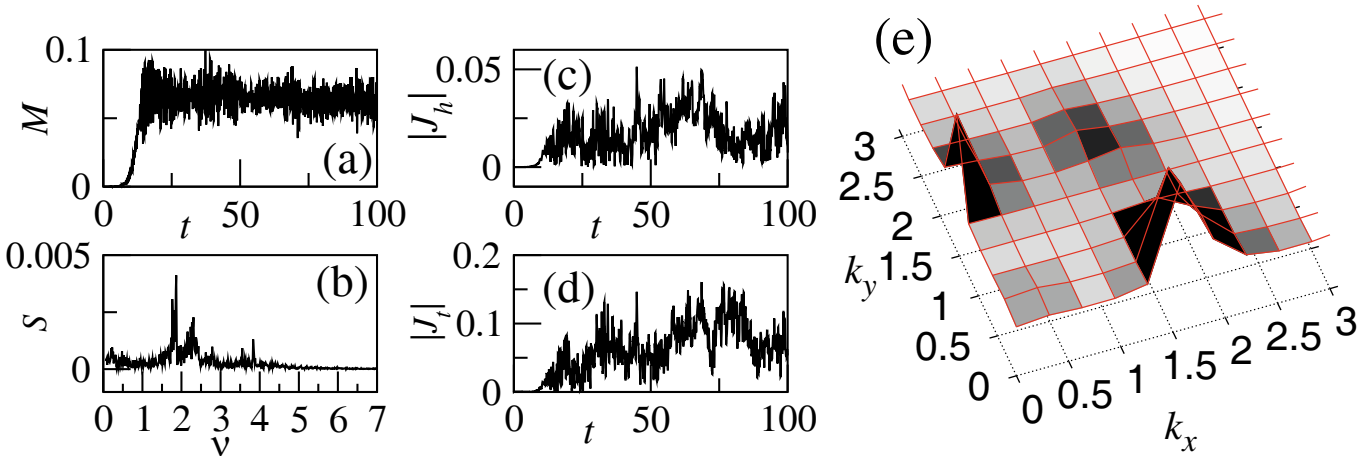

Fig. 8. (Color online) Temporal evolution from the homogeneous state for parameters as in fig. 7. (a) The mode type M, (b) the spectral density $S(\nu)$ of $M(t)$ on the interval $t \in [20, 100]$, (c) the magnitude of the fluid flux, $|\bar{J}_h| = \sqrt{(\bar{J}_h)_x^2 + (\bar{J}_h)_y^2}$, (d) the magnitude of the translational flux of the swimmers, $|\bar{J}_t| = \sqrt{(\bar{J}_t)_x^2 + (\bar{J}_t)_y^2}$, and (e) the time-averaged power spectral density of the height profile obtained with eq. (B.2) by averaging over the interval $t \in [50, 100]$.

Finally, to reveal the periodic structure of the pattern, we show in fig. 8(e) the time-averaged power spectral density (for $t \in [50, 100]$) introduced in eq. (B.2) of appendix B. It has two major broad peaks: one at ($k_x = 2\pi m/L = 1.57$, $k_y = 2\pi k/L = 0$), *i.e.* $m = 5$, $k = 0$, and one at ($k_x = 2\pi m/L = 0$, $k_y = 2\pi k/L = 1.57$), *i.e.* $m = 0$ and $k = 5$. They correspond to a square pattern with the main lattice directions aligned along the coordinate axes, *i.e.* $\Psi = 0$ or $\Psi = \pi/2$. The dominating wave length or lattice constant l_w of the pattern is $l_w = L/\sqrt{m^2 + k^2} = 20/5 = 4$. The third peak with much smaller intensity at ($k_x = 2\pi m/L = 1.25$, $k_y = 2\pi k/L = 1.88$), *i.e.*, $m = 4$ and $k = 6$, can be interpreted as a contribution from the sum of the two dominant wave vectors spanning the reciprocal lattice.

4.4 Multistability

To systematically study the occurrence and stability of the two discussed patterns we follow them in parameter space using a primitive "continuation method". Namely, we take a snapshot of a converged (time-dependent) state at some parameter value and use it as initial condition for a simulation at a nearby parameter value. This technique allows us to follow states which are linearly stable and thereby to identify multistable regions in parameter space. Depending on the initial condition different stable spatio-temporal stable patterns are obtained. For an overview of proper continuation methods, which are also able to follow unstable steady states and therefore to determine the complete bifurcation diagram, see refs. [64,65]. However, these

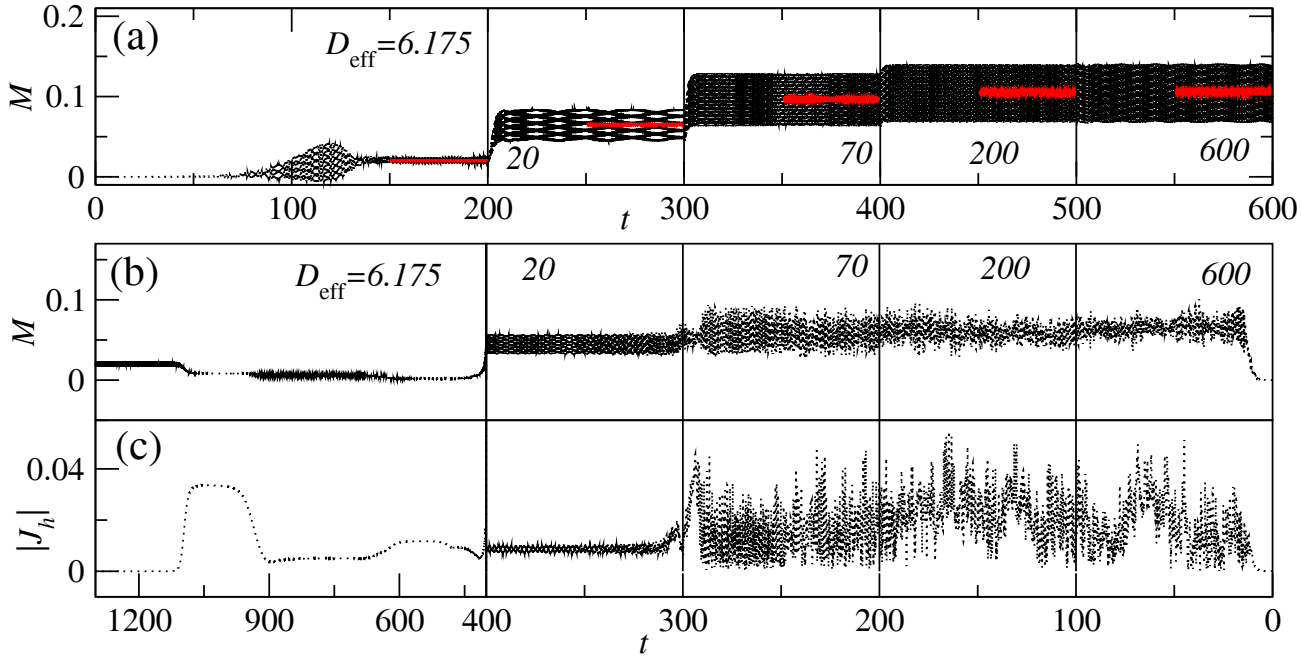

Fig. 9. (Color online) (a) The mode number M during the continuation of the standing waves at fixed $V = 3.5$ and $L = 20$. Standing waves that emerged from the homogeneous steady state at $V = 3.5$ and $D_{\text{eff}} = 6.175$ are numerically continued by increasing D_{eff}. The vertical lines mark times when D_{eff} is changed. The respective values of D_{eff} for each interval are given by the numbers in each panel. The thick red solid line shows the mode type, averaged over one oscillation period. (b,c) Continuation of patterns with intermittent symmetry, emerged from the homogeneous steady state at $V = 3.5$ and $D_{\text{eff}} = 600$ with $L = 20$. Shown are (b) the mode number M and (c) the modulus of the fluid flux $\sqrt{(\bar{J}_h)_x^2 + (\bar{J}_h)_y^2}$ in dependence of time. The time axis is reversed.

methods are not readily available for time-periodic solutions of our PDE system. First, we start with the regular standing wave pattern, explored in sect. 4.2. We follow the standing wave solution along the line connecting points 2 and 4 in fig. 2(a) by decreasing D (increasing D_{eff}) in steps, namely, $D_{\text{eff}} = 6.175 \to 20 \to 70 \to 200 \to 600$. At each point, we let the system settle into a stable state, which we identify by monotoring $M(t)$ and $\bar{J}_h$. The resulting time evolution of mode type M during the continuation schedule is shown in fig. 9(a). We find that the standing wave pattern keeps its main characteristics up to the largest value $D_{\text{eff}} = 600$ (point 4 in fig. 2(a)). In particular, M shows regular oscillations. $\bar{M}$ (red solid line in fig. 9(a)) and the oscillation amplitude of M increase with D_{eff}. They reach their respective maximal values of 0.1 and 0.06 at around $D_{\text{eff}} = 200$, where the density and height variations are more pronounced than in fig. 5. Furthermore, the oscillation period monotonically increases with D_{eff} (not shown). The spatial period remains unchanged.

Next, we start with the strongly perturbed square pattern from sect. 4.3 and follow the same path in fig. 2(a) but this time backward from point 4 to point 2. For consistency, we use the same values of D_{eff} as in fig. 9(a). The time evolutions of M and $|\bar{J}_h|$ are plotted in figs. 9(b) and (c) with reversed time axis. Remarkably, the system reaches the regular standing wave pattern only for parameters close to the stability threshold, *i.e.*, when D_{eff} is decreased to the value in point 2 in fig. 2(a). There, after a transient dynamics, from $t = 400$ to 1100 the system settles on the stable standing wave pattern.

For larger values of D_{eff}, *i.e.*, further away from the threshold, we found that the system is multistable. At $D_{\text{eff}} > 20$ stable regular standing waves still exist but also patterns similar to the strongly perturbed square pattern in fig. 7 are stable. However, at $D_{\text{eff}} = 20$, the dynamics of the square pattern becomes more regular but still keeps the feature of lattice planes splitting and merging with their neighbors. This is demonstrated by Movie-3 in the Supplementary material and by the snapshots in fig. 10(a) and (b), taken at $t = 400$. Figure 10(c) shows the x and y components of the translational flux of the swimmers. One clearly recognizes directed motion, on average, into the negative x and positive y direction. The components of $\bar{J}_h(t)$ behave similarly. Furthermore, both flux components show a fast oscillation with a superimposed weak slow modulation. By taking the Fourier transforms of $|\bar{J}_h(t)|$ (fig. 10(d)), one identifies a dominant peak at $\nu = 3.5$ corresponding to a period of $T = 0.28$ of the fast oscillations. They result from the pulsation in the square pattern as Movie-3 demonstrates. The weak modulation generates a small peak in the power spectrum with frequency $\nu = 0.36$ or period $T = 2.8$. The continuous part of the spectrum as observed in fig. 8(b) for the strongly perturbed square pattern is missing here since the square pattern has a more regular dynamics.

Finally, the time-averaged power spectral density S_h, for $t \in [350, 400]$, is given in fig. 10(e). The two major

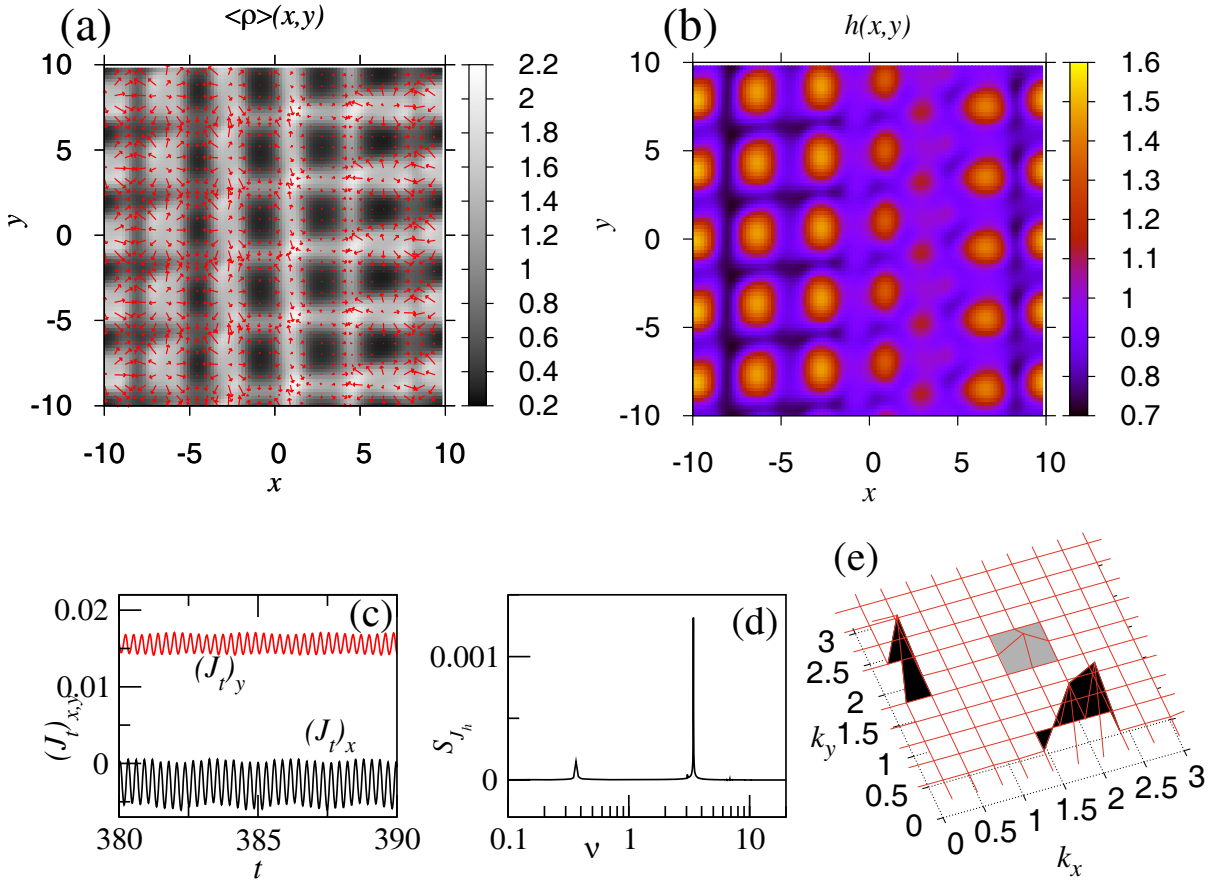

Fig. 10. (Color online) (a,b) Persisting dynamic state at $V = 3.5$ and $D_{\text{eff}} = 20$, during the numerical continuation of the patterns with intermittent symmetry in fig. 9. Snapshot taken at $t = 400$. (c) The components of the translational surface flux $\bar{J}_t$. (d) The spectral density of $|\bar{J}_h|(t)$. (e) Time-averaged power spectral density of the pattern, obtained with eq. (B.2) by averaging over the interval $t \in [350, 400]$.

peaks correspond to the square pattern with spatial period of $L/6$ aligned along the coordinate axes. The third, much weaker peak at $k_x = k_y = 2\pi m/L = 1.57$ with $m = 5$ again corresponds to a contribution of the two major wave vectors spanning the reciprocal lattice.

4.5 Persisting traveling patterns

In the triangular mixed instability region in fig. 2 one finds persisting travelling waves characterized by a time-independent mode type and a constant non-zero fluid flux. Figures 11(a) and (b) give snapshots obtained at point 3 in fig. 2(a) for $L = 20$ and $t = 900$. Movie-4 in the Supplementary material shows the pattern travels approximately along the diagonal with a propagation speed approximately equal to the self-propulsion velocity $V = 2$. The maxima of h form a rectangular lattice. Perturbations run along the lattice lines and shift the maxima by roughly half a lattice constant; presumably, to match the periodic BC. The time evolutions of M, $(J_h)_x$ and $(J_h)_y$ are shown in fig. 11(c) and (d), respectively. The height modulation at an arbitrary point plotted in fig. 11(e) looks rather irregular. Its power spectrum in fig. 11(f) has a peak at $\nu = 0.32$, which corresponds to single shift motions of a bump in the height profile. Frequencies at $\nu = 0.1$ and 0.17 belong to longer cycles of two or three shifts. The power spectral density for the spatial modulations in the film height, averaged over the interval $t \in [800, 900]$, is plotted in fig. 11(g). In the snapshot in fig. 11(b) one can clearly see a rectangular pattern with the aspect ratio of ≈ 1.3. Remarkably, it is not compatible with the periodic BC of the square domain. Nontheless, the pattern fits into the domain due to the presence of a defect-like modulation, seen at the center of the snapshot. It disturbes the rectangular lattice dynamically, as it continuously moves along the lattice lines and shifts the elevations in the height profile (see Movie-4). As a result, in the power spectrum in fig. 11(g) we find two major peaks located at $\{k_x^{(1)} = 0.62, k_y^{(1)} = 1.25\}$ and $\{k_x^{(2)} = -0.94, k_y^{(2)} = 0.62\}$ and one smaller peak located at $\{k_x^{(3)} = -0.94, k_y^{(3)} = 0.31\}$. The remaining two weaker peaks are again higher order contributions.

4.6 Random patterns

When studying the nonlinear behaviour for $V = 3.5$ and $D_{\text{eff}} = 0.66$ (point 1 in fig. 2(a)), we find truly random

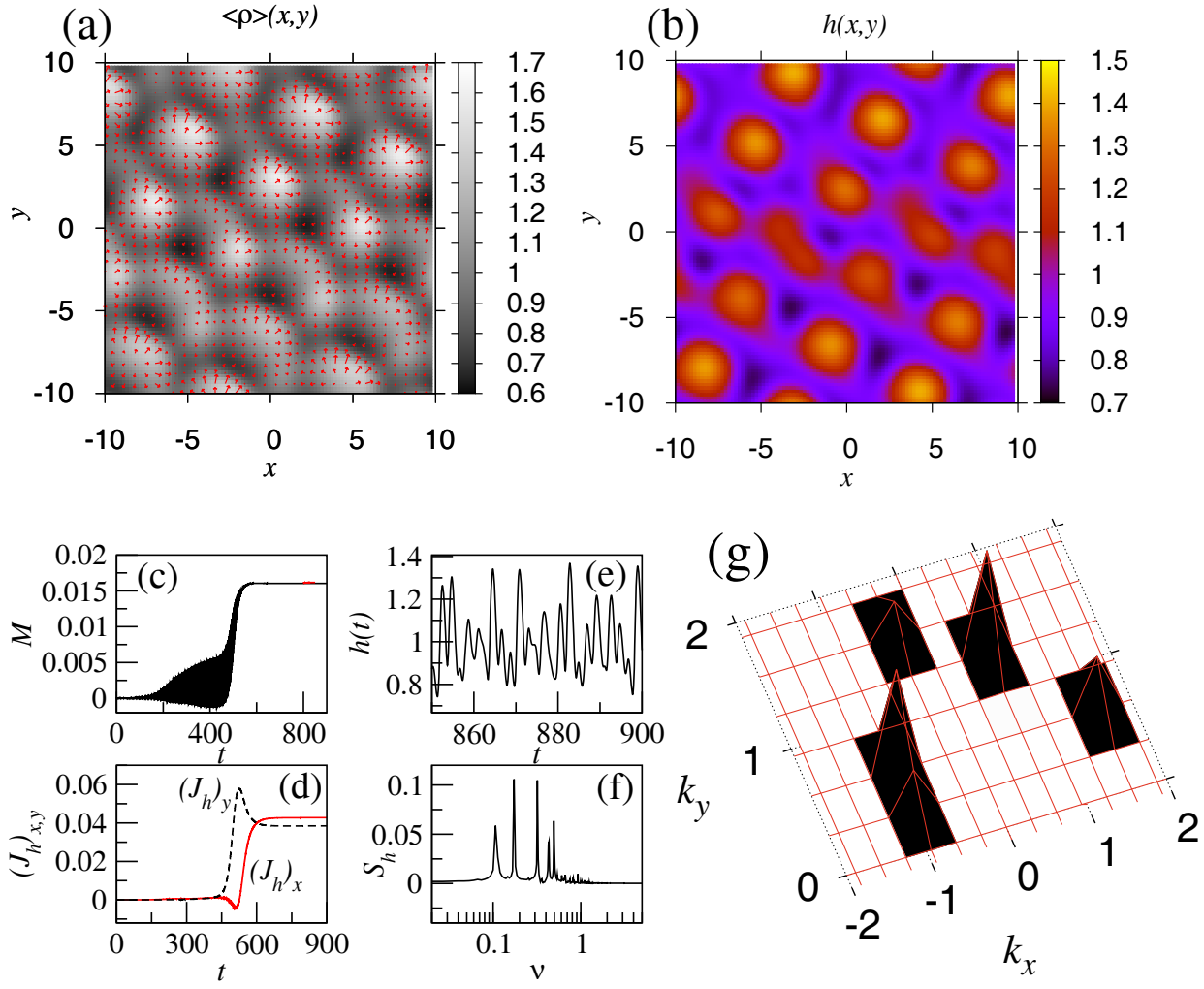

Fig. 11. (Color online) (a,b) Snapshots of the persisting traveling pattern, which emerges from the mixed instability type for $V = 2$, $D = 2.4$, ($D_{\text{eff}} = 0.88$), $L = 20$ (see point 3 in fig. 2(a)). The corresponding dispersion curve is shown in fig. 2(d). (c) Mode type M, (d) x and y component of the space averaged fluid flux $\bar{\boldsymbol{J}}_h$, (e) the film height $h(t)$ at a randomly chosen point on the film surface, and (f) its power spectrum S_h. (g) Power spectrum for the spatial modulation of the height profile (see eq. (B.2)) averaged over the interval $t \in [800, 900]$.

patterns emerging from the zero-wave-number instability. The corresponding dispersion curve is shown in fig. 2(b) and gives $l_{\max} \approx 9$. We set $L = 60$, $N = 128$ and start the simulations at the trivial state. After a transient, the system settles onto an irregular spatio-temporal pattern that oscillates randomly and locally travels in random directions. Typical snapshots are shown in fig. 12 and movie-5 in the Supplementary material illustrates the irregular dynamics.

The randomness is clearly visible in the time evolution of M and $|\bar{J}_h|$, shown in figs. 13(a) and (b), respectively. The time-averaged power spectral density S_n in fig. 13(a) is radially symmetric (implying that spatial correlations in the pattern only depend on the distance r between any two points) and has a pronounced maximum at $|\boldsymbol{k}| = 0.7$. Otherwise, it is continuous as expected for a random pattern. Via the convolution theorem, S_n is directly related to the spatial height correlation function

$$C(\boldsymbol{r}) = \frac{C_0}{t_2 - t_1} \int_{t_1}^{t_2} \mathrm{d}t \int [h(\boldsymbol{r}+\boldsymbol{w})-1][h(\boldsymbol{w})-1]\mathrm{d}\boldsymbol{w}, \quad (34)$$

where $t_1 = 150$ and $t_2 = 350$ and the constant C_0 is chosen such that $C(0) = 1$. We plot the normalised radially symmetric correlation function $C(r)$ in fig. 13(f). $C(r)$ rapidly decreases with r and drops by two orders of magnitude over the distance of $r = 10$, as shown in the inset of fig. 13(f). Correlations become negligibly small at distances larger than 10 and the pattern looks random. The oscillation at small distances corresponds to the maximum in the power spectral density. They are caused by wave fronts traveling in random directions, which one recognizes in the orientation-averaged swimmer density in movie-5. Finally, the film height at an arbitrary position

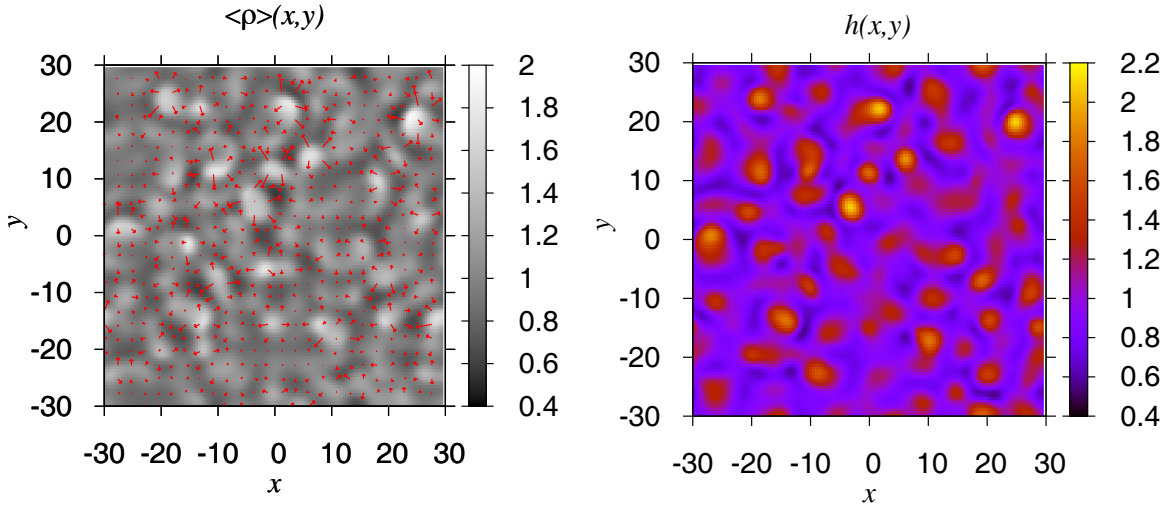

Fig. 12. (Color online) Random patterns emerge in the region of the zero-wave-number instability at $V = 3.5$ and $D_{\text{eff}} = 0.66$ in a system of size $L = 60$. Number of the Fourier modes for the discretisation in space is $N = 128$.

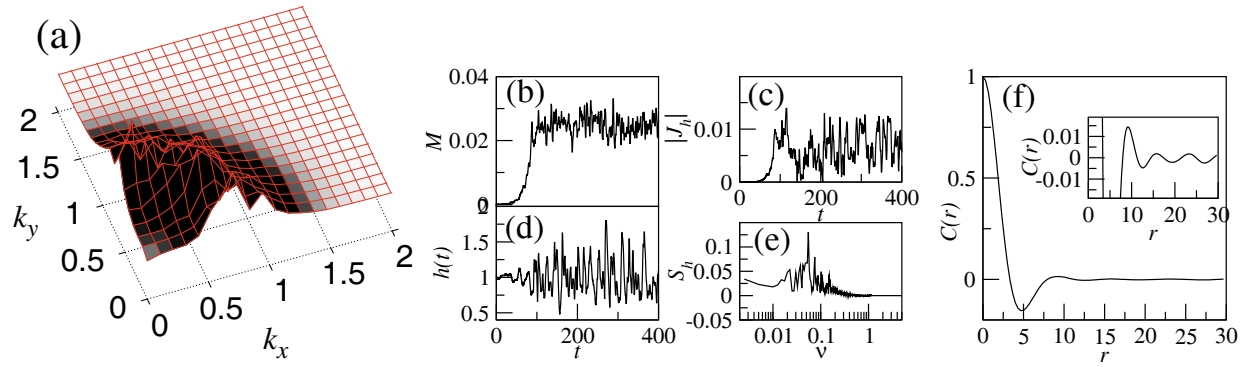

Fig. 13. (Color online) (a) Time-averaged spectral density from eq. (B.2) computed numerically by averaging the Fourier transformed film thickness patterns in fig. 12 over $t \in [150, 350]$. (b,c) The mode type M and the modulus of the fluid flux $|\bar{J}_h|$ over time. (d) Time evolution of $h(t)$ at a randomly chosen point on the film surface. (e) Spectral density S_h of $h(t)$ from (d). (f) Normalised radial autocorrelation function $C(r)$. Inset shows zoomed graph of $C(r)$ around zero.

changes randomly in time, as shown in fig. 13(d). However, the spectral density S_h plotted in fig. 13(e) has a clear peak at $\nu = 0.055$. This implies that the temporal dynamics of the patterns cannot be regarded as purely random.

5 Discussion and conclusion

We have investigated the collective behaviour of a colony of point-like non-interacting self-propelled particles (micro-swimmers) that swim at the free surface of a thin liquid layer on a solid support. In contrast to ref. [39], where the motion of the swimmers was considered to be purely orthogonal to the free surface, here we have also allowed for active motion parallel to the film surface. The resulting coupled dynamics of the swimmer density $\rho(x, y, \phi, t)$ and the film thickness profile $h(x, y, t)$ is captured in a long-wave model in the form of a Smoluchowski equation for the one-particle density $\rho(x, y, \phi, t)$ and a thin-film equation for $h(x, y, t)$ that allows for i) diffusive and convective transport of the swimmers (including rotational diffusion), ii) capillarity effects (Laplace pressure) including a Marangoni force caused by gradients in the swimmer density, iii) and a vertical pushing force of the swimmers that acts onto the liquid-gas interface.

First, we have extended the linear stability analysis of the homogeneous and isotropic state of ref. [40] focusing on the characteristics of the two distinct instability modes (zero- and finite-wave-number mode). We have found that the onset and dispersion relation of the zero-wave-number mode do not fit well into the classification scheme of Cross and Hohenberg [60]. The long-wave instability occurs at $k = 0$, where the two leading eigenvalues are always real. However, arbitrarily close above onset, the fastest growing mode is oscillatory. Moreover, the unstable band of wave numbers, $0 < k < k_c$, does *always* contain a range at small $k < k_{\text{rc}} \sim |\eta|$ (with η measuring the distance from the stability threshold), where the two leading eigenvalues are real (one $\sim k^2$ and one $\sim k^4$), and a range $k_{\text{rc}} < k < k_c$,

where they form a complex conjugate pair. This indicates that this zero-wave-number instability is similar to a zero-frequency Hopf bifurcation in dynamical systems [64] and in the context of the instabilities of spatially extended systems, it might be called a zero-frequency type II_0 instability.

The behaviour at about $k = 0$ has also important implications for a weakly nonlinear theory for the short-wave instability at $k = k_c$. Such a theory would need to take into account that the slow complex modes around $k = k_c$ couple to the two stable or unstable long-wave modes at $k \approx 0$ with real eigenvalues. We believe that such a coupling is responsible for the observed wave behaviour, where a travelling wave is perturbed by a long-wave modulation, as in fig. 10. The two long-wave modes are a direct consequence of the existing two conserved quantities in the system: the mean film height and the orientation-averaged mean swimmer concentration. Simpler cases with one long-wave mode (resulting from a single conserved quantity) that couples to a short-wave mode have been considered in refs. [73–75]. Such an analysis is not feasible in our case, where the evolution equations capture the dynamics in two spatial dimensions *and* account for a fully ϕ-dependent density $\rho(x, y, \phi, t)$. However, a one-dimensional model system, where instead of rotational diffusion the swimmers can only flip between swimming to the left or right shows similar transitions and lends itself to a weakly nonlinear analysis. Such a simplified system is under investigation and will be presented elsewhere.

We have employed numerical simulations of the time evolution eqs. (8) and (12) to give an overview of the rich variety of persisting dynamic states. In particular, for parameters close to the stability threshold of the finite wave number instability, we have found a regular standing wave pattern that oscillates between square and stripe patterns. Spatial variations of the film thickness profile and the orientation-averaged density profile are in-phase implying that high density spots sit approximately on top of the droplets. The orientation of swimmers in each high density spot shows strong polar order with a hedgehog defect right at the center. The space-averaged fluid flux of the square wave is always zero.

In systems of active matter, stable square patterns have previously been found in Vicsek-type models with memory. It was shown that in the case of a ferromagnetic alignment between the self-propelled particles with memory in the orientational ordering the system settles to a perfectly symmetric state with a checkerboard arrangement of clockwise and anti-clockwise vortices [25]. Using our classification, this checkerboard lattice corresponds to a square pattern with the main axis tilted by $\Psi = \pi/4$ w.r.t. the coordinate axes. Rectangular (nearly quadratic) positional order has also been reported as a state of collective dynamics in an active particle model with competing alignment interaction [26, 57]. A similar oscillation between stripe and square patterns as found here was reported for a mesoscopic continuum model for an active filament-molecular motor system where the oscillation is described as alternating wave between aster-like states that form a square lattice and stripe states [58]. A related analysis of steady stripe and aster states is presented in [59].

Experiments with active matter often find hexagonal patterns. For instance, a hexagonal lattice of vortices was observed in suspensions of highly concentrated spermatozoa of sea urchins [8]. Phenomenologically, the existence of hexagonal patterns is often studied using a Swift-Hohenberg (SH) equation for scalar fields [60,61]. For such model equations it is known that hexagonal structures can only be stable if the model equations are not invariant under inversion of the scalar field and that higher-order gradient terms are needed to stabilize square patterns [62, 63]. In our case, inversion symmetry is broken, *i.e.*, eqs. (8) and (12) are not invariant under the simultaneous transformations $h \to -h$ and $\rho \to -\rho$. Nevertheless, in our numerical simulations we have not found stable hexagonal patterns but find that square patterns dominate. This could imply that higher order terms play an important role. Alternatively it may indicate that a SH equation is not the appropriate order parameter equation for our model that in contrast to the standard variational SH equation has no gradient dynamics structure (see discussion in sect. 2 below eq. (12)).

Furthermore, we have employed a "primitive" continuation method and have followed the standing wave patterns through parameter space and have shown that standing wave patterns exist and are stable possibly in the entire region, where the homogeneous state is linearly unstable w.r.t. the finite wave number instability (*i.e.* for $D_{\rm eff} > 1$). A strongly perturbed square pattern, where lattice lines continuously split and merge with their neighbors emerges from the trivial state at large $D_{\rm eff}$. This state also persists for an extended range of $D_{\rm eff}$ resulting in a range of multistability.

Multistability of several persisting dynamic states under identical external conditions was also found in other systems. For example, in experiments on groups of schooling fish [66] it was observed that depending on the starting conditions and/or the nature of perturbations, as well as the group size, a fish swarm may exhibit two different dynamic states: the so-called milling state, which is characterized by fish swimming in a large circle, and the polarised state, which corresponds to fish swimming predominantly in one direction.

In the mixed-instability region, we find a persisting traveling wave pattern characterised by constant space-averaged fluid flux. Elevations in the film surface are arranged in a rectangular lattice that travels in one direction with the speed of the order of the self-propulsion velocity, while perturbations continuously shift the hight elevations. At their positions the swimmers form high-density spots with strong polar order around a hedgehog defect similar to the regular standing wave. Finally, choosing parameters from the region with the zero-wave-number instability, one finds a random spatio-temporal pattern with a correlation length much smaller than the system size.

Persisting propagating structures are well known for other active matter systems. Thus, traveling density waves

were found in experiments with an assay of actin filaments, driven by motor proteins [20]. At the leading edge (lamellipodium) of a crawling cell, the alignment of actin filaments along the substrate leads to the forward translation of lamellipodium and thus, to cell motility [67]. Moving density stripes and propagating isolated density clusters have been found in microscopic Vicsek-type models and in continuum models of self-propelled particles [68–70]. Highly dynamic random spatio-temporal patterns of active matter are known as quasi or mesoscale turbulence. Irregular turbulent states have been found in experiments with dense bacterial suspensions [10–16, 19] and in active microtubuli networks [71].

Our findings clearly show that a rich variety of persisting regular and irregular dynamic states can be found in an active matter system of self-propelled particles without direct interactions. In our model, the interaction between the swimmers occurs on a coarse-grained level and is mediated by large-scale deformations of the liquid film. Similar types of dynamic states were previously observed in other active matter systems of interacting particles as indicated above. It is fascinating that active particles acting as surfactants at the surface of a thin liquid film provide a model system, where all these different dynamic patterns can be realized by tuning appropriate parameters.

Possible extensions of the model include the incorporation of wettability effects by adding the Derjaguin (disjoining) pressure to study swimmer carpets not only on films but also on shallow droplets and, in particular, interactions with (moving) contact lines. One may also go beyond the approximation of point-like non-interacting particles by introducing finite size effects (short-range interactions between particles) as well as long-range (hydrodynamic) interactions. The resulting Smoluchowski equation would then contain non-local terms as in dynamical density functional theories for the diffusive dynamics of interacting colloids, polymers, and macromolecules [76,77]. For a consistent model also the film height equation would require additional terms that may be determined via the gradient dynamics formulation [38] that has to be recovered in the limit of passive surfactant particles/molecules.

Appendix A. Semi-implicit numerical scheme for eqs. (12), (8)

In the employed dimensionless quantities, the resulting coupled system consists of the reduced Smoluchowski equation and the thin-film equation. It reads

$$\begin{aligned} \partial_t h + \boldsymbol{\nabla}\cdot\boldsymbol{J}_h &= 0,\\ \partial_t \rho + \boldsymbol{\nabla}\cdot\boldsymbol{J}_{\mathrm{t}} + \partial_\phi J_\phi &= 0, \end{aligned} \tag{A.1}$$

with the dimensionless fluid flux $\boldsymbol{J}_h$, the translational and rotational probability currents $\boldsymbol{J}_t$ and J_ϕ, the surface fluid velocity $\boldsymbol{U}_\parallel$ and the vorticity of the fluid flow Ω_z

$$\begin{aligned} \boldsymbol{J}_h &= \frac{h^3}{3}\boldsymbol{\nabla}\left[\Delta h + \beta\langle\rho\rangle\right] - \frac{1}{2}\left(h^2\boldsymbol{\nabla}\langle\boldsymbol{\rho}\rangle\right),\\ \boldsymbol{J}_{\mathrm{t}} &= \left(V\boldsymbol{q} + \boldsymbol{U}_\parallel - d\boldsymbol{\nabla}\right)\rho,\\ J_\phi &= \frac{1}{2}\Omega_z\rho - D\partial_\phi\rho,\\ \boldsymbol{U}_\parallel &= -h\boldsymbol{\nabla}\langle\rho\rangle + \frac{h^2}{2}\boldsymbol{\nabla}\left(\Delta h + \beta\langle\rho\rangle\right),\\ \Omega_z &= \partial_x U_y - \partial_y U_x. \end{aligned} \tag{A.2}$$

The coupled eqs. (A.1) are solved numerically using the following version of the semi-implicit spectral method. First, we average the density equation over the orientation angle ϕ. This yields

$$\partial_t\langle\rho\rangle + \boldsymbol{\nabla}\cdot\langle\boldsymbol{J}_{\mathrm{trans}}\rangle = 0, \tag{A.3}$$

with the average translational current $\langle\boldsymbol{J}_{\mathrm{trans}}\rangle = V\langle\boldsymbol{q}\rho\rangle + (\boldsymbol{U} - d\boldsymbol{\nabla})\langle\rho\rangle$ and $\boldsymbol{q} = (\cos\phi, \sin\phi)$. It is worthwhile noticing that the only term in eq. (A.3) that depends on the three-dimensional density $\rho(x, y, \phi, t)$ is the average orientation vector $\langle\boldsymbol{q}\rho\rangle$. All other terms in eq. (A.3), including the surface fluid velocity $\boldsymbol{U}$ explicitly depend on the average density $\langle\rho\rangle$. Next, we group the thin-film equation together with eq. (A.3)

$$\begin{aligned} \partial_t h + \boldsymbol{\nabla}\cdot\boldsymbol{J}_h &= 0,\\ \partial_t\langle\rho\rangle + \boldsymbol{\nabla}\cdot\langle\boldsymbol{J}_{\mathrm{trans}}\rangle &= 0, \end{aligned} \tag{A.4}$$

with the fluid flux $\boldsymbol{J}_h = \frac{h^3}{3}\boldsymbol{\nabla}[\Delta h + \beta\langle\rho\rangle] - \frac{1}{2}\boldsymbol{\nabla}(h^2\boldsymbol{\nabla}\langle\boldsymbol{\rho}\rangle)$. At the next step, we single out the linear parts in all the terms in eqs. (A.4) that explicitly depend on the average density $\langle\rho\rangle$. This is done by linearising the current $\boldsymbol{J}_t$ and the fluid flux $\boldsymbol{J}_h$ about the trivial steady state given by $h = 1$ and $\langle\rho\rangle = 1$. Finally, following the standard implicit time-integration scheme, we replace $\partial_t h$ and $\partial_t\langle\rho\rangle$ by $(h^{t+\mathrm{d}t} - h^t)/\mathrm{d}t$ and by $(\langle\rho\rangle^{t+\mathrm{d}t} - \langle\rho\rangle^t)/\mathrm{d}t$, respectively and take all linear terms at time $t + \mathrm{d}t$ and all nonlinear terms, including the term $V\langle\boldsymbol{q}\rho\rangle$, at time t. Upon these transformations eqs. (A.4) become

$$\begin{aligned} &\frac{h^{t+\mathrm{d}t} - h^t}{\mathrm{d}t} + \frac{1}{3}\Delta^2 h^{t+\mathrm{d}t} + \left(\frac{\beta}{3} - \frac{1}{2}\right)\Delta\langle\rho\rangle^{t+\mathrm{d}t}\\ &\quad + \boldsymbol{\nabla}\cdot(\boldsymbol{N}\boldsymbol{L}_h)^t = 0,\\ &\frac{\langle\rho\rangle^{t+\mathrm{d}t} - \langle\rho\rangle^t}{\mathrm{d}t} + \frac{1}{2}\Delta^2 h^{t+\mathrm{d}t} + \left(\frac{\beta}{2} - 1 - d\right)\Delta\langle\rho\rangle^{t+\mathrm{d}t}\\ &\quad + \boldsymbol{\nabla}\cdot(\langle\boldsymbol{N}\boldsymbol{L}_{\mathrm{trans}}\rangle)^t = 0, \end{aligned} \tag{A.5}$$

with the nonlinear parts given by

$$\begin{aligned} (\boldsymbol{N}\boldsymbol{L}_h)^t &= \Bigg[\frac{h^3 - 1}{3}\boldsymbol{\nabla}\left[\Delta h + \beta\langle\rho\rangle\right]\\ &\qquad - \frac{1}{2}\boldsymbol{\nabla}\left([h^2 - 1]\boldsymbol{\nabla}\langle\boldsymbol{\rho}\rangle\right)\Bigg]^t,\\ (\langle\boldsymbol{N}\boldsymbol{L}_{\mathrm{trans}}\rangle)^t &= \Bigg[V\langle\boldsymbol{q}\rho\rangle + (\boldsymbol{U})\langle\rho\rangle - \frac{1}{2}\boldsymbol{\nabla}(\Delta h)\\ &\qquad - \left(\frac{\beta}{2} - 1\right)\boldsymbol{\nabla}\langle\rho\rangle\Bigg]^t. \end{aligned} \tag{A.6}$$

After taking the discrete Fourier transforms of eqs. (A.5), we find the updated fields $h^{t+\mathrm{d}t}$ and $\langle\rho\rangle^{t+\mathrm{d}t}$ at the time step $t+\mathrm{d}t$. With the update average density $\langle\rho\rangle^{t+\mathrm{d}t}$ and the film thickness $h^{t+\mathrm{d}t}$ at hand, we find the updated surface fluid velocity $\boldsymbol{U}^{t+\mathrm{d}t}$ and the updated vorticity $\Omega^{t+\mathrm{d}t}$. These functions are then substituted into the three-dimensional density equation

$$\frac{\rho^{t+\mathrm{d}t}-\rho^{t}}{\mathrm{d}t}+\boldsymbol{\nabla}\cdot\boldsymbol{J}_{\mathrm{trans}}+\partial_{\phi}J_{\mathrm{rot}}=0, \tag{A.7}$$

with the translational current $\boldsymbol{J}_{\mathrm{trans}} = V(\boldsymbol{q}\rho)^{t} + (\boldsymbol{U}^{t+\mathrm{d}t})\rho^{t} - d\boldsymbol{\nabla}\rho^{t+\mathrm{d}t}$ and the rotational current $J_{\phi} = (1/2)\Omega^{t+\mathrm{d}t}\rho^{t} - D(\partial_{\phi}\rho^{t+\mathrm{d}t})$. After taking the Fourier transform of eq. (A.7) both, in space as well as in the angle ϕ, we find the updated three-dimensional density $\rho^{t+\mathrm{d}t}$.

Appendix B. Analysis of square pattern

The spatial period l_w of the standing wave discussed in sect. 4.2 can be determined in real space by measuring the distance between two nearest maxima (minima) of the square pattern in the height profile $h(x,y)$. The maximal error in this procedure is of the order of $\sqrt{2}L/N$ where N is the number of discretization points along the x and y axis and the factor $\sqrt{2}$ reflects that the wave is directed along the diagonal of the domain. We obtain $l_w = 3.5 \pm 0.14$ for the square pattern in fig. 5 using $L = 20$ and $N = 100$ to estimate the error.

Due to the periodic BC the measured l_w is slightly different from the linear fastest growing wave length $l_{\max} = 2\pi/k_{\max} = 3.43$ (fig. 2(b)) as explained next. To fulfill periodic boundary conditions in a square domain of size L, the periods of a wave projected, respectively, on the x and y axis are L/k and L/m, where m and k are some integers. This restricts the possible rotation angles Ψ of a periodic pattern relative to the x axis (see fig. 5). They have to satisfy

$$\cos\Psi = \frac{m}{\sqrt{k^2+m^2}}\,, \qquad \sin\Psi = \frac{k}{\sqrt{k^2+m^2}} \tag{B.1}$$

and the wave length of the pattern becomes $l_w = L/\sqrt{k^2+m^2}$. Thus, for the parameters used in fig. 5, the random initial conditions select the possible rotation angle $\Psi = \pi/4$. This choice corresponds to $m = k$ in eq. (B.1). Next, the integer $m = 4$ is chosen in such a way that the resulting wave length of the pattern, $l_w = L/(m\sqrt{2}) = 3.53$, is close to the fastest growing wave length of $l_{\max} = 3.43$.

For later use, we mention that the spatial period l_w and the angle Ψ of a simulated periodic pattern can be determined by computing the time-averaged power spectral density of the film thickness profile $h(x,y,t)$ according to

$$S_h(\boldsymbol{k}) = \frac{1}{T}\int_{t}^{t+T} |\hat{h}(\boldsymbol{k})|^2\,\mathrm{d}t, \tag{B.2}$$

where T is the temporal period of oscillations and $\hat{h}(\boldsymbol{k})$ denotes the discrete Fourier transform of $h(x,y,t)$. The periodic boundary conditions for the square domain only allow for a discrete set of possible wave vectors forming a square lattice with lattice constant $\Delta k = 2\pi/L \approx 0.31$. Any periodic pattern in the height modulation $h(x,y)$ gives a major peak of the power spectrum in eq. (B.2), which is located at $k_x = 2\pi m/L$, $k_y = 2\pi k/L$, with the same integers m and k as in eq. (B.1). Depending on the surface profile, secondary peaks (higher harmonics) might be present, but their strengths are typically orders of magnitude smaller compared to the major peak.

Author contribution statement

All authors contributed equally to the paper.

References

1. S. Ramaswamy, Annu. Rev. Condens. Matter Phys. **1**, 323 (2010).
2. M. Marchetti, J. Joanny, S. Ramaswamy, T. Liverpool, J. Prost, M. Rao, R. Simha, Rev. Mod. Phys. **85**, 1143 (2013).
3. I. Buttinoni, J. Bialké, F. Kümmel, H. Löwen, C. Bechinger, T. Speck, Phys. Rev. Lett. **110**, 238301 (2013).
4. I. Theurkauff, C. Cottin-Bizonne, J. Palacci, C. Ybert, L. Bocquet, Phys. Rev. Lett. **108**, 268303 (2012).
5. J. Palacci, C. Cottin-Bizonne, C. Ybert, L. Bocquet, Phys. Rev. Lett. **105**, 088304 (2010).
6. J. Palacci, S. Sacanna, A.P. Steinberg, D.J. Pine, P.M. Chaikin, Science **339**, 936 (2013).
7. S. Thutupalli, R. Seemann, S. Herminghaus, New J. Phys. **13**, 073021 (2011).
8. I.H. Riedel, K. Kruse, J. Howard, Science **309**, 300 (2005).
9. C. Dombrowski, L. Cisneros, S. Chatkaew, R.E. Goldstein, J. Kessler, Phys. Rev. Lett. **93**, 098103 (2004).
10. E. Lushia, H. Wioland, R.E. Goldstein, Proc. Natl. Acad. Sci. U.S.A. **111**, 9733 (2005).
11. A. Sokolov, I.S. Aranson, J.O. Kessler, R.E. Goldstein, Phys. Rev. Lett. **98**, 158102 (2007).
12. A. Sokolov, I.S. Aranson, Phys. Rev. Lett. **109**, 248109 (2012).
13. K.-A. Liu, L. I, Phys. Rev. E **86**, 011924 (2012).
14. A. Sokolov, R.E. Goldstein, F.I. Feldchtein, I.S. Aranson, Phys. Rev. E **80**, 031903 (2009).
15. H.H. Wensink, J. Dunkel, S. Heidenreich, K. Drescher, R.E. Goldstein, H. Löwen, J.M. Yeomans, Proc. Natl. Acad. Sci. U.S.A. **109**, 14308 (2012).
16. T. Ishikawa, N. Yoshida, H. Ueno, M. Wiedeman, Y. Imai, T. Yamaguchi, Phys. Rev. Lett. **107**, 028102 (2011).
17. C. Dombrowski, L. Cisneros, S. Chatkaew, R.E. Goldstein, J.O. Kessler, Phys. Rev. Lett. **93**, 098103 (2004).
18. J. Schwarz-Linek, C. Valeriani, A. Cacciuto, M.E. Cates, D. Marenduzzo, A.N. Morozov, W.C.K. Poon, Proc. Natl. Acad. Sci. U.S.A. **109**, 4052 (2012).
19. J. Dunkel, S. Heidenreich, K. Drescher, H.H. Wensink, M. Bär, R.E. Goldstein, Phys. Rev. Lett. **110**, 228102 (2013).
20. V. Schaller, C. Weber, C. Semmrich, E. Frey, A.R. Bausch, Nature **467**, 73 (2010).
21. T. Surrey, F. Nédélec, S. Leibler, E. Karsenti, Science **292**, 1167 (2001).

22. Y. Sumino, K.H. Nagai, Y. Shitaka, D. Tanaka, K. Yoshikawa, H. Chate, K. Oiwa, Nature **483**, 448 (2012).
23. I. Derenyi, T. Vicsek, Phys. Rev. Lett. **75**, 374 (1995).
24. A. Bricard, J.-B. Caussin, N. Desreumaux, O. Dauchot, D. Bartolo, Nature **503**, 95 (2013).
25. K.H. Nagai, Y. Sumino, R. Montagne, I.S. Aranson, H. Chaté, Phys. Rev. Lett. **114**, 168001 (2015).
26. R. Großmann, P. Romanczuk, M. Bär, L. Schimansky-Geier, Phys. Rev. Lett. **113**, 258104 (2014).
27. E. Lauga, T.R. Powers, Rep. Prog. Phys. **72**, 096601 (2009).
28. J. Bialke, H. Löwen, T. Speck, EPL **103**, 30008 (2013).
29. F. Peruani, A. Deutsch, M. Bär, Phys. Rev. E **74**, 030904 (2006).
30. A. Baskaran, M.C. Marchetti, Phys. Rev. E **77**, 011920 (2008).
31. S. van Teeffelen, H. Löwen, Phys. Rev. E **78**, 020101(R) (2008).
32. A. Zöttl, H. Stark, Phys. Rev. Lett. **112**, 118101 (2014).
33. M. Hennes, K. Wolff, H. Stark, Phys. Rev. Lett. **112**, 238104 (2014).
34. O. Pohl, H. Stark, Phys. Rev. Lett. **112**, 238303 (2014).
35. O. Pohl, H. Stark, Eur. Phys. J. E **38**, 93 (2015).
36. I.S. Aranson, A. Sokolov, J.O. Kessler, R.E. Goldstein, Phys. Rev. E **75**, 040901 (2007).
37. G. Subramanian, D.L. Koch, J. Fluid Mech. **632**, 359 (2009).
38. U. Thiele, A.J. Archer, M. Plapp, Phys. Fluids **24**, 102107 (2012).
39. S. Alonso, A. Mikhailov, Phys. Rev. E **79**, 061906 (2009).
40. A. Pototsky, U. Thiele, H. Stark, Phys. Rev. E **90**, 030401(R) (2014).
41. A. Oron, S. Davis, S. Bankoff, Rev. Mod. Phys. **69**, 931 (1997).
42. L.W. Schwartz, D.E. Weidner, R.R. Eley, Langmuir **11**, 3690 (1995).
43. V. Garbin, J.C. Crocker, K.J. Stebe, Langmuir **28**, 1663 (2012).
44. D. Alizadehrad, T. Krüger, M. Engstler, H. Stark, PLoS Comput. Biol. **11**, e1003967 (2015).
45. J.R. Howse, R.A.L. Jones, A.J. Ryan, T. Gough, R. Vafabakhsh, R. Golestanian, Phys. Rev. Lett. **99**, 048102 (2007).
46. L. Helden, R. Eichhorn, C. Bechinger, Soft Matter **11**, 2379 (2015).
47. T. Lee, M. Alarcon-Correa, C. Miksch, K. Hahn, J. Gibbs, P. Fischer, Nano Lett. **14**, 2407 (2014).
48. M. Enculescu, H. Stark, Phys. Rev. Lett. **107**, 058301 (2011).
49. K. Wolff, A. Hahn, H. Stark, Eur. Phys. J. E **36**, 43 (2013).
50. C.W. Gardiner, *Handbook of Stochastic Methods* (Springer-Verlag, Berlin Heidelberg, 2004).
51. A. Pototsky, H. Stark, EPL **98**, 50004 (2012).
52. E. Stellamanns, S. Uppaluri, A. Hochstetter, N. Heddergott, M. Engstler, T. Pfohl, Sci. Rep. **4**, 6515 (2014).
53. J. Palacci, C. Cottin-Bizonne, C. Ybert, L. Bocquet, Phys. Rev. Lett. **105**, 088304 (2010).
54. B. ten Hagen, S. van Teeffelen, H. Löwen, J. Phys.: Condens. Matter **23**, 194119 (2011).
55. R. Golestanian, Phys. Rev. Lett. **108**, 038303 (2012).
56. P. Beltrame, U. Thiele, SIAM J. Appl. Dyn. Syst. **9**, 484 (2010).
57. R. Grossmann, P. Romanczuk, M. Bar, L. Schimansky-Geier, Eur. Phys. JST **224**, 1325 (2015).
58. F. Ziebert, Ph.D. thesis, Universität Bayreuth (2006).
59. F. Ziebert, W. Zimmermann, Eur. Phys. J. E **18**, 41 (2005).
60. M.C. Cross, P.C. Hohenberg, Rev. Mod. Phys. **65**, 851 (1993).
61. J. Dunkel, S. Heidenreich, M. Bär, R.E. Goldstein, New J. Phys. **15**, 045016 (2013).
62. M. Bestehorn, *Hydrodynamik und Strukturbildung: Mit einer kurzen Einfuhrung in die Kontinuumsmechanik (Springer-Lehrbuch) (German Edition)* (Springer, 2006), ISBN 3540337962.
63. R.A. Meyers, *Encyclopedia of Complexity and Systems Science*, Vol. **4** (Springer-Verlag, New York, 2009) p. 3611, ISBN 978-0-387-30440-3.
64. Y.A. Kuznetsov, *Elements of Applied Bifurcation Theory*, 3rd ed. (Springer, New York, 2010).
65. H.A. Dijkstra, F.W. Wubs, A.K. Cliffe, E. Doedel, I.F. Dragomirescu, B. Eckhardt, A.Y. Gelfgat, A. Hazel, V. Lucarini, A.G. Salinger *et al.*, Commun. Comput. Phys. **15**, 1 (2014).
66. K. Tunstrøm, Y. Katz, C.C. Ioannou, C. Huepe, M.J. Lutz, I.D. Couzin, PLoS Comput. Biol. **9**, 1 (2013).
67. J.V. Small, Th. Stradal, E. Vignal, K. Rottner, Trends Cell Biol. **12**, 112 (2002).
68. H. Chaté, F. Ginelli, G. Grégoire, F. Peruani, F. Raynaud, Eur. Phys. J. B **64**, 451 (2008).
69. A. Gopinath, M.F. Hagan, M.C. Marchetti, A. Baskaran, Phys. Rev. E **85**, 061903 (2012).
70. S. Mishra, A. Baskaran, M.C. Marchetti, Phys. Rev. E **81**, 061916 (2010).
71. T. Sanchez, D.T.N. Chen, S.J. DeCamp, M. Heymann, Z. Dogic, Nature **491**, 431 (2012).
72. Y. Kuznetsov, *Elements of Applied Bifurcation Theory* (Springer-Verlag, New York, 2004).
73. P.C. Matthews, S.M. Cox, Nonlinearity **13**, 1293 (2000).
74. S.M. Cox, P.C. Matthews, Physica D **175**, 196 (2003).
75. D. Winterbottom, P. Matthews, S. Cox, Nonlinearity **18**, 1031 (2005).
76. U.M.B. Marconi, P. Tarazona, J. Chem. Phys. **110**, 8032 (1999).
77. A.J. Archer, R. Evans, J. Chem. Phys. **121**, 4246 (2004).